

Effect of Transition Modeling for Analysis of a Slotted, Natural-Laminar-Flow Transonic Truss-Braced Wing Aircraft Configuration

Cody Perkins*, Zhi Yang†, and Dimitri Mavriplis‡
University of Wyoming, Laramie, WY 82070, United States

James G. Coder§, and Chris Axten¶
Penn State University, University Park, PA 16802, United States

Lawton Shoemake||
General Dynamics Information Technology, Washington D.C. 20375, United States

The integration of a slotted, natural-laminar-flow (SNLF) airfoil with a transonic truss-braced wing (TTBW) configuration has been shown to offer significant benefits in comparison to other widely implemented designs for commercial transport applications. This work focuses on the computational analysis of the S207 SNLF airfoil and associated TTBW configuration and wind tunnel model. The performance of this airfoil is largely dependent on the duration of laminar flow maintained across the chord length. Thus proper prediction of the transition from laminar to turbulent flow is of top priority. Computations are performed using two closely related Reynolds-averaged Navier-Stokes (RANS) solvers operating on unstructured grids. Results using both the single-equation Menter and Two-Equation Amplification Transport (AFT2) transition prediction models are compared, with the latter demonstrating laminar flow behavior more representative of S207 airfoil design intent. Results acquired for an S207-based wind tunnel model were compared to experimental results and showed notable differences. Efforts to identify sources of these discrepancies lead to further two-dimensional and three-dimensional investigation in which transition prediction model parameters were varied. A complete set of drag polars over a range of Mach numbers was obtained for the S207 TTBW configuration demonstrating the ability to predict overall trends in performance with free transition for laminar flow aircraft designs.

I. Introduction

The use of aircraft on both a commercial and individual basis has grown in popularity and, consequently, is playing a progressively larger role in the global warming crisis. The International Energy Agency (IEA) reported a 126.6% increase in international aviation energy consumption between 1990 and 2017, with the United States attaining a growth of 89.4% [1]. Additionally, the use of private aircraft alone can result in 7500 tons of emitted CO₂ per year[2]. In response to the rise of aircraft generated pollutants, and other factors shaping the needs of the aviation industry, the NASA Aeronautics Research Mission Directorate (ARMD) has formulated six thrusts that set forth aircraft technology research and development intentions for the near-term (N+1), mid-term (N+2), and far-term (N+3)[3]. Specifically, the third thrust details improvements to subsonic commercial aircraft, making them more economically viable, less noisy, and more environmentally conscious. Technology associated with N+3 metrics will contribute to a fleet-level net reduction in emissions of 50% compared to a 2005 baseline by 2050[3].

A laminar boundary layer is associated with much lower skin friction drag (C_f) in comparison to a turbulent boundary layer. Laminar flow has thus become a targeted mechanism for enhanced aircraft efficiency for vehicles ranging in

*MS Student, Department of Mechanical Engineering, AIAA Member; Email: cperki12@uwyo.edu

†Research Scientist, Department of Mechanical Engineering, AIAA Member; Email:ZYang@uwyo.edu

‡Professor, Department of Mechanical Engineering, AIAA Fellow; Email: mavripl@uwyo.edu

§Associate Professor, Department of Aerospace Engineering, AIAA Senior Member; Email: jcoder@psu.edu

¶MS Student, Department of Mechanical Aerospace Engineering, AIAA Member; Email: cja5217@psu.edu

||Computational Engineer, AIAA Member; Email: Lawton.Shoemake@gdit.com

size and speed capabilities. More specifically, the development and application of natural-laminar-flow (NLF) airfoils has seen some success in reducing drag and fuel burn through establishing extensive runs of laminar flow across the chord length of the wing. Through careful shaping of the airfoil cross section, a NLF wing establishes a favorable pressure gradient as far aft as possible, achieving laminar flow on the upper and lower surfaces for about 70% the chord length[4–8].

Further developments have been made on the front of laminar flow technology. Slotted, natural-laminar-flow (SNLF) airfoils were first patented in 2005[5] and seek to improve upon the performance of NLF airfoils. SNLF airfoils differ from NLF airfoils through the addition of an aft element, introducing design considerations characterized by the flow present between the two elements, a region more commonly referred to as the slot. The flow through the slot facilitates a favorable pressure gradient on the upper surface of the fore element, as the trailing-edge pressure of the fore element is no longer required to recover to the freestream value due to the presence of the aft element[6–9]. This pressure gradient stabilizes the boundary layer, offering two distinct benefits. First, laminar flow is theoretically achieved for the entire chord length of the fore element and a notable portion of the aft element, reducing the C_f value even further than what a NLF airfoil is capable of[5–8]. Second, wing profile drag, or drag produced due to boundary layer separation on the wing, is reduced as the stabilization of the boundary layer due to the favorable pressure gradient prevents flow detachment. In the context of commercial transport vehicles, this becomes incredibly beneficial as wing profile drag accounts for roughly a third of the total drag (C_D) acting on the vehicle[6–8]. Additionally, SNLF technology lends itself to a lighter aircraft. It is less complex mechanically, structurally, and operationally than other profile drag reduction techniques such as active laminar flow control[6–8]. The study of already existing SNLF geometries offers testament to the technology’s benefits. The S204 SNLF airfoil was designed for business jet applications and was able to achieve high maximum lift and low profile drag goals based on initial computational analysis[7]. The S414 SNLF airfoil was proposed for rotor-craft applications, and met high maximum lift and low profile drag objectives through both computational analysis and wind tunnel testing[10, 11]. Furthermore, comparison of these results to those associated with the single-element, NLF counterpart of the S414 airfoil highlighted the benefit of the slot.

The extensive runs of laminar flow enabled by both NLF and SNLF type airfoils is beneficial to the performance of an aircraft if implemented properly. The presence of this laminar regime can be quantified through examination of the drag polar, where the formation of a low-drag bucket can be observed. This low-drag bucket is characterized by a minimum in C_D (or C_f) across a wide range of lift coefficient (C_L) values. It is bounded by the upper and lower C_L conditions, beyond which a significant increase in drag is observed. This is due to the movement of the boundary layer transition line further upstream, resulting in increased turbulence. An example of the low-drag bucket’s likeness can be viewed in Figure 1a.

The S207 SNLF airfoil is a 13.49%-thick SNLF airfoil designed for transonic commercial transport applications[8, 9]. It is insensitive to roughness and computational results acquired using MSES[12], as outlined in the original design report, predict the upper and lower C_L low-drag bucket limits to be 0.37 and 0.74, respectively, for a Mach number of 0.700 and a Reynolds number of 13.2 million[8]. The maximum C_L value is computed to be 2.13 at a Mach number of 0.225 and a Reynolds number of 16.0 million[8]. The profile of the S207 SNLF airfoil is included as Figure 1b. Design metrics for this airfoil were derived from the Boeing Mach 0.745 Transonic Truss-Braced Wing (TTBW) aircraft[9], a concept that utilizes a large aspect ratio wing and was designed under the Subsonic Ultra Green Aircraft Research (SUGAR) initiative[13]. It has been found that pairing the S207 airfoil with a TTBW structure can theoretically decrease block fuel per seat by 58% compared to a SUGAR free baseline geometry[9]. Efforts conducted under the Advanced Aerodynamics Design Center for Ultra-Efficient Commercial Vehicles, which is a NASA funded University Leadership Initiative (ULI) led by the University of Tennessee at Knoxville, are focused on the extensive analysis of a S207-based SNLF TTBW vehicle configuration with the goal being a 70% reduction in fuel and energy burn compared to 2005 standards[14]. The project concluded this year and completed work has demonstrated the superior performance this vehicle offers in comparison to modern aircraft[15]. This paper summarizes tasks completed in support of the ULI through computational analysis of the S207 airfoil and associated TTBW configuration and is a continuation of efforts presented in previous work[16].

II. Methodology

A. Predicting Transition

This work concerns itself with the use of two transition prediction models. The first is the single-equation Menter model[17]. This model draws its foundation from the concept of Local-Correlation-based Transition Modeling (LCTM)

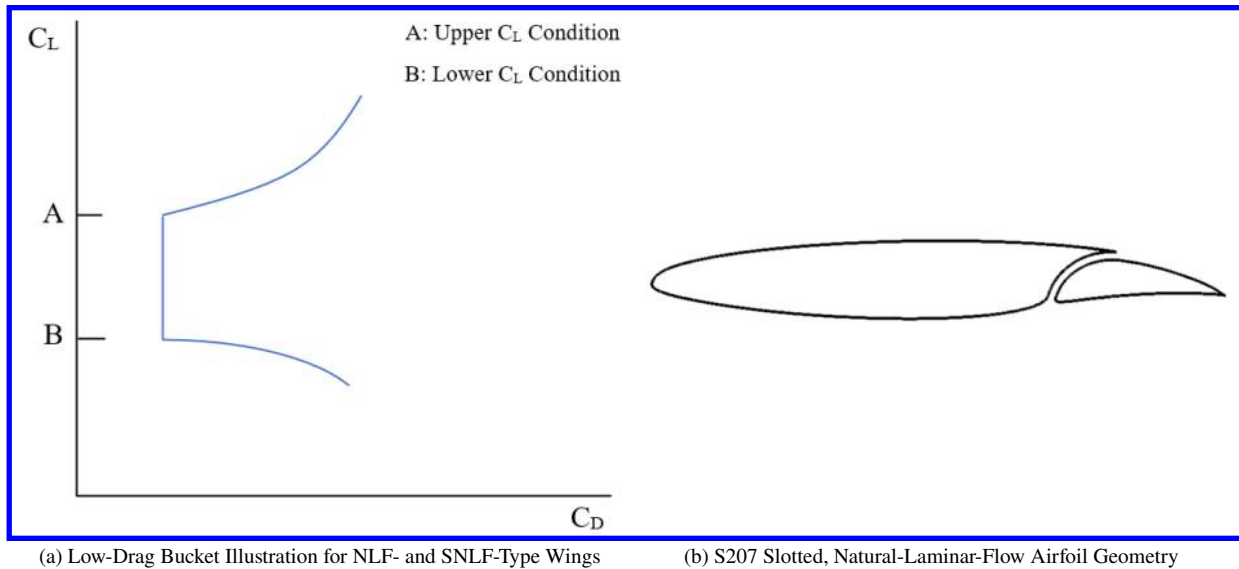


Fig. 1 Relevant SNLF Airfoil Characteristics

and is an improvement on the two-equation γ -Re model[18, 19]. The need for the Re-equation is removed, making the model exclusively dependent on the turbulence intermittency (γ) for triggering the transition from laminar to turbulent flow. The second is the Two-Equation Amplification Factor Transport (AFT2 or AFT2019) model[20]. Founded on linear stability theory, the model computes the progression of the amplification factor associated with streamwise instabilities. This transport equation is coupled with an intermittency equation as well. The transition criterion is met once the maximum amplification ratio of any considered instability in the boundary layer reaches a specific value denoted N_{crit} . This parameter can be used as a direct input or computed from freestream turbulence intensity (Tu_∞) using Mack's relationship[20, 21]. It is necessary to note that these models do not account for crossflow instabilities. This mechanism becomes more relevant with increasing wing sweep and is dominant when wing sweep is above 15° [9]. The SNLF wing analyzed under ULI project efforts was intentionally designed to have a sweep of 12.5° to minimize concern for crossflow instabilities. This design decision validates the use of the AFT2 and Menter transition prediction models for use in this work. Both models have been implemented into our RANS solvers[22].

B. Solutions in Two Dimensions

In this work, two-dimensional CFD analyses were performed using NSU2D[23]. NSU2D is an in-house developed steady-state code that solves the compressible RANS equations on unstructured grids. The NSU2D spatial discretization method is a central difference scheme with added matrix-based dissipation and is nominally second-order accurate. An efficient multigrid scheme can be utilized to accelerate convergence, but various other solver modules are available as well. Modeling capabilities include various turbulence models and transition prediction. Two-dimensional results presented in this work are computed using either the Spalart-Allmaras (SA) turbulence model[24] alone or with a coupled SA-AFT2 implementation[22]. The AFT2 model parameter N_{crit} is computed from an input for Tu_∞ . Grids for the 2D CFD analyses performed in this work were generated using UMESH2D[25], a code associated with the NSU2D software package.

C. Solutions in Three Dimensions

The three-dimensional CFD simulations performed in this work were completed using NSU3D[26]. Like NSU2D, this software is a steady-state RANS solver, and it extends the schemes, accuracy, and capabilities of its predecessor to three dimensions. NSU3D is compatible with various grid formats including hybrid grids that have various cell types. The code has been extensively validated through its use in previous high-lift, drag prediction and aeroelastic prediction workshops[27–29]. The three-dimensional CFD analyses performed in this work include data generated from approaches utilizing either the Menter model or the AFT2 model for transition prediction, and only the SA model for turbulence modeling. The AFT2 model parameter N_{crit} is used as a direct input. Grids for the three-dimensional

geometries were generated by members of the ULI at the University of Tennessee at Knoxville using the Pointwise software.

A patch- and box-based modeling specification capability was implemented into NSU3D as part of this work. This allows the selected free transition model or turbulence model to be applied to the surface of the aircraft based on patch identifiers and a distance value, or to regions of the domain bounded by specified points. These implementations can both overlap and override each other through a priority number. Figure 2 visually details this capability through an example where the first 3% chord is intended to be modeled as free transition and the remaining chord length is fully turbulent.

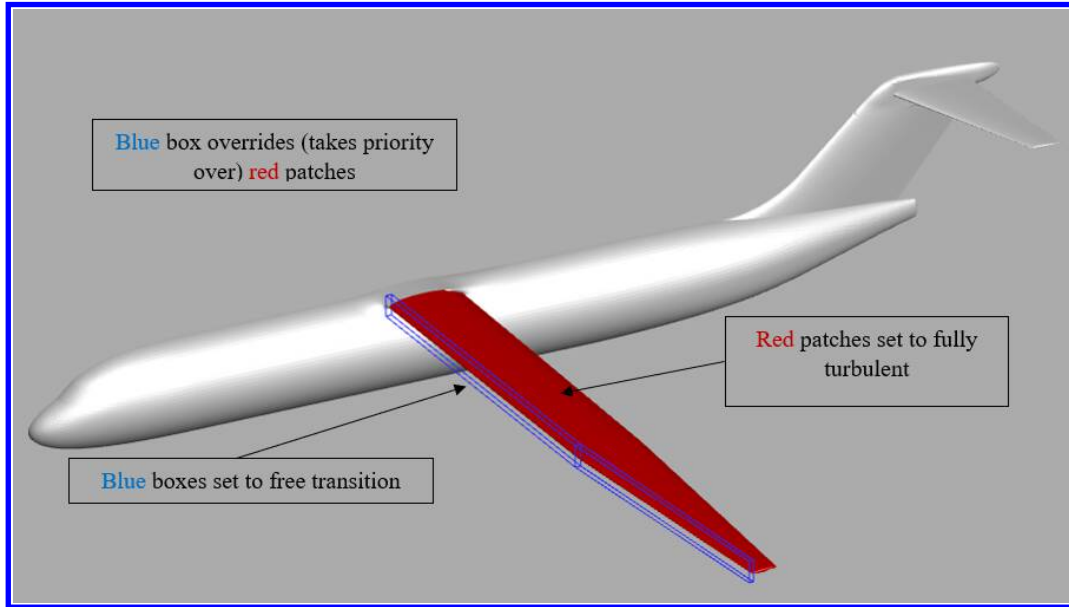


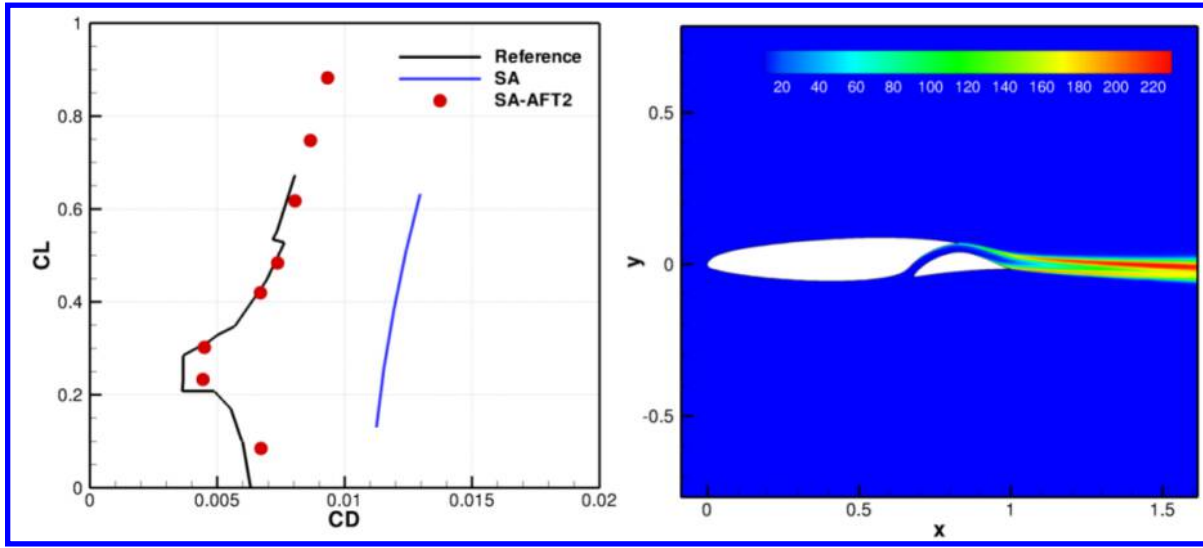
Fig. 2 Patch- & Box-Based Modeling Implementation Example: Free Transition Up to 3% Chord

D. Validation Efforts

Validation of the transition prediction implementations associated with NSU2D and NSU3D, as well as the application of an optimization framework to SNLF technology, was conducted under the ULI[30]. Results from the free transition validation efforts are reproduced herein. The NSU2D AFT2 model was validated through study of the S204 SNLF airfoil. The low-drag bucket for this SNLF airfoil is bounded by C_L values of approximately 0.2 and 0.4, with slight variations for different Reynolds numbers[7]. Figure 3a illustrates the NSU2D results computed with and without the use of the AFT2 model compared to the design polar for a Mach number of 0.5 and Reynolds number of 12×10^6 . A Tu_∞ value of 0.07%, which corresponds to an N_{crit} value of 9.0, was used in the case of free transition, and these results show close agreement with reference data[7]. Furthermore, adequate capture of the low-drag bucket is achieved. A contour plot of eddy viscosity for the free transition solution is included as Figure 3b and suggests that laminar flow is maintained for a large percentage of the chord length.

The TU Braunschweig sickle wing transition experiment was selected for testing the performance of the NSU3D free transition modeling capabilities[30]. Results using both the Menter and AFT2 models were compared to data associated with the original experiment[31] and a solution acquired using OVERFLOW[20], a RANS solver that operates on overset structured grids, for a Mach number of 0.5, an α of -2.6° , and a Reynolds number of 2.5 Million. Figure 4 illustrates this comparison for the upper surface of the wing. Figure 5 does the same for the lower surface. Overall, transition locations on the upper surface predicted by NSU3D using both the Menter and AFT2 models agree qualitatively with those presented in reference[20]. Lower surface transition locations do appear to be predicted slightly downstream with NSU3D, but within acceptable margins.

NSU3D has been utilized for problems associated with SNLF TTBW configurations as well, as results for a notional S204-based three-dimensional TTBW configuration with free transition are presented in reference[30]. This analysis included the effects of coupled aero-structural displacements[32], and a subsequent twist distribution optimization was



(a) Comparison to Reference[7]

(b) Eddy Viscosity for $\alpha = 0^\circ$

Fig. 3 NSU2D Results for the S204 Airfoil at Mach = 0.5, $Re = 12.0 \times 10^6$, and $Tu_\infty = 0.07\%$

performed. However, optimization and aero-structural analysis were not exercised in the current work for the S207-based SNLF TTBW configuration. It should be noted that the notional character of the S204-based TTBW configuration precluded the availability of preexisting computational or experimental data for validation purposes.

III. Effect of Transition in Two Dimensions

A. Initial Results in Two Dimensions for the S207 Airfoil

Initial efforts in analyzing the S207 airfoil began by establishing correspondence between an NSU2D generated solution and MSES data set forth in the S207 airfoil design report[8]. The grid used for analysis of the S207 airfoil in NSU2D has been discussed previously in reference[16], and its characteristics are reproduced herein. This S207 airfoil grid is unstructured with 689,326 triangular cells in total. The far-field boundaries are located a distance of 1,000 chord lengths in each coordinate direction. Both the fore and the aft elements have 2,000 surface points. Streamwise spacing at the leading-edges and trailing-edges is set to 0.02% the chord length to ensure adequate refinement in these areas, and the normal wall-spacing for both elements is 10^{-6} chord lengths. The growth rate of the cells nearest the airfoil body is 1.1 in order to capture the expected thin laminar boundary layer. Images of the grid are included in Figure 6.

The upper and lower C_L conditions for the low-drag bucket of the S207 airfoil at a Mach number of 0.7 and a Reynolds number of 13.2 million were predicted by MSES to be 0.37 and 0.74, respectively[8]. The associated C_D in the region of the low-drag bucket is roughly 0.0027 to 0.0029. Note that a Tu_∞ of 0.07%, which corresponds to a N_{crit} value of 9.0, was used for the transition prediction equations in these MSES runs. A simulation at an identical Mach number and Reynolds number, a lower Tu_∞ of 0.001% ($N_{crit} = 19.2$), and an angle of attack (α) of -1.3° was completed in NSU2D. This simulation is denoted as Run 1 and required a restart from a fully turbulent simulation that was run for 100 cycles as starting from freestream values resulted in numerical divergence. Run 1 predicted a C_L value of 0.658 and a C_D value of 0.00318[16], falling within close proximity to the MSES computed low-drag bucket values.

Though Run 1 was successful in establishing agreement between MSES and NSU2D, its Tu_∞ value of 0.001% is much lower than the 0.07% ($N_{crit} = 9.0$) value used in MSES. A second simulation was completed using NSU2D with this higher Tu_∞ value, and is denoted as Run 2. The flow parameters for Run 2 were the same as those used in Run 1. Specifically, the Mach number was 0.7, the Reynolds number was 13.2 million, and α was -1.3° . The simulation was again started from a flow field acquired from 100 fully turbulent cycles. The final C_L and C_D computed for Run 2 are 0.620 and 0.0035, respectively. These values are again within proximity to the low-drag bucket values computed by MSES and presented in the S207 airfoil design report[8]. Additionally, the C_L is lower and the C_D is higher than the values computed in Run 1, which is to be expected for the higher Tu_∞ value.

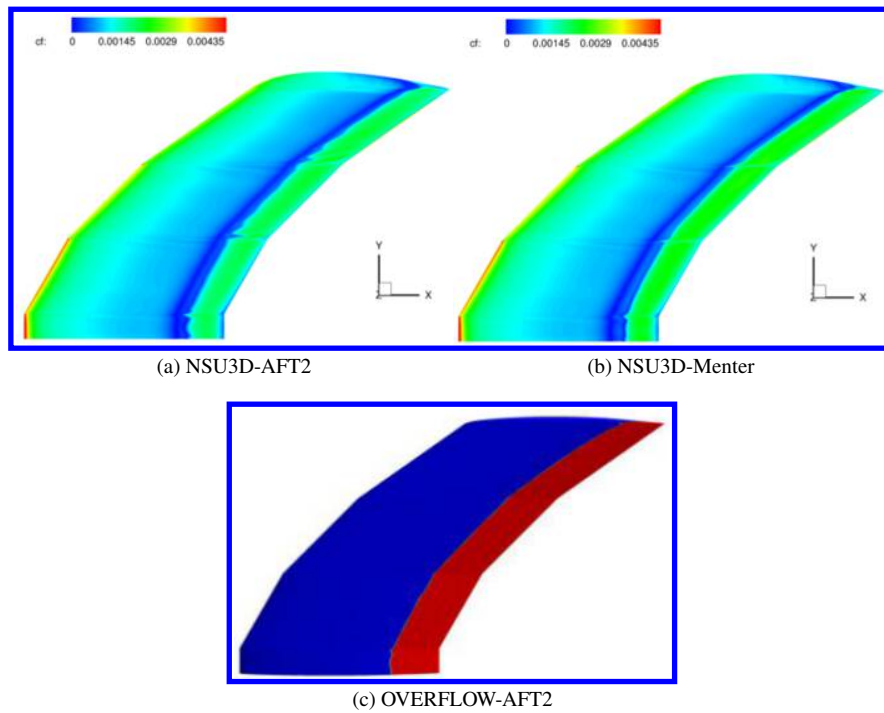


Fig. 4 Upper Surface Transition Location Comparison for Mach = 0.156, $\alpha=-2.6^\circ$ and $Re=2.7 \times 10^6$: NSU3D vs. OVERFLOW

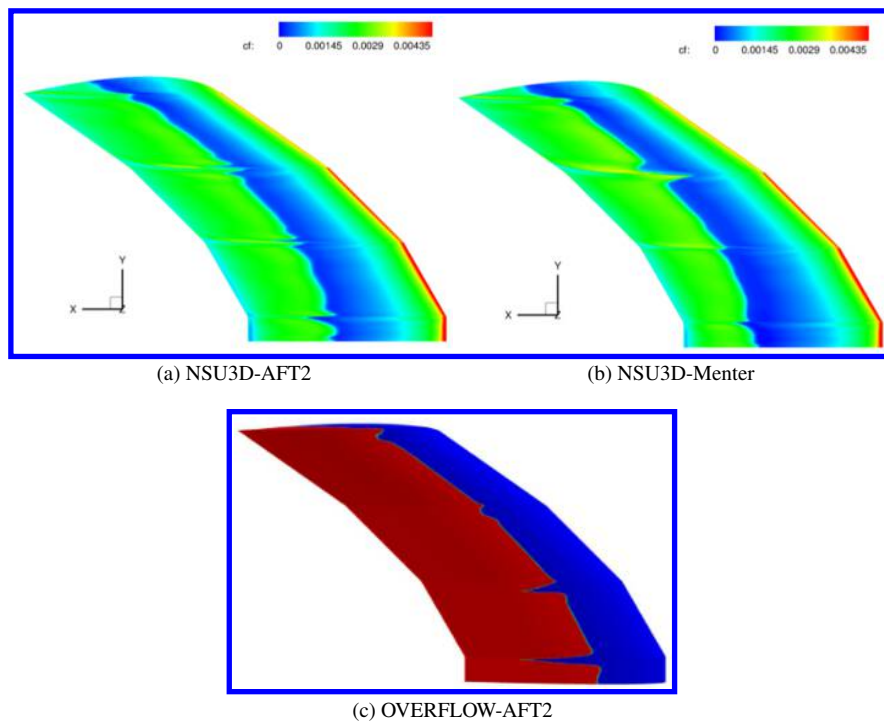


Fig. 5 Lower Surface Transition Location Comparison for Mach = 0.156, $\alpha=-2.6^\circ$ and $Re=2.7 \times 10^6$: NSU3D vs. OVERFLOW

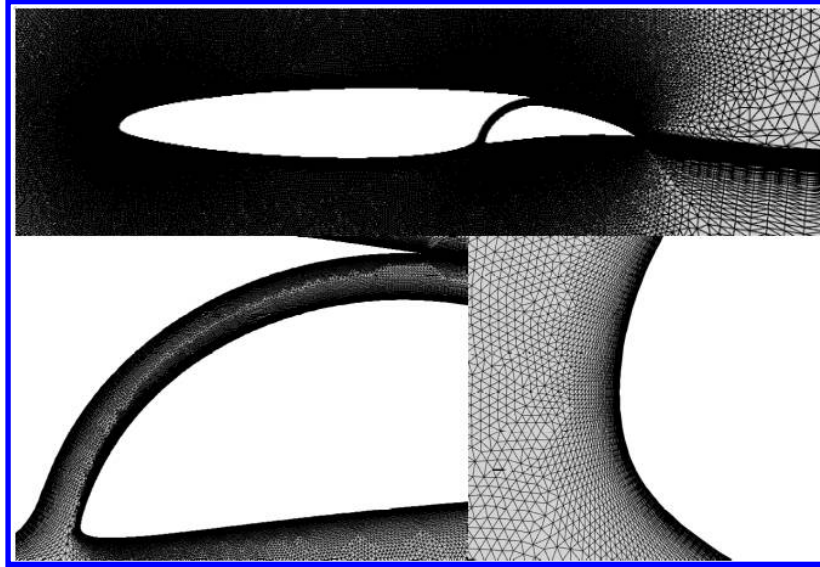


Fig. 6 S207 Airfoil Grid used for Analysis in NSU2D

Both Run 1 and Run 2 were successful in establishing agreement between NSU2D RANS solutions and MSES design results, however, an important aspect of their approach is a freeze of the transition prediction equations. Run 1 was executed for 10000 cycles and Run 2 was executed for 20000 cycles, and in both cases the AFT2 transition model was frozen after 3250 cycles. This aided in driving down the mean flow and turbulence model residuals, as convergence stagnation was observed when freezing of the transition prediction model was not invoked. This transition freeze strategy was used previously for ULI work in the development of a free transition, adjoint-based optimization framework for an S204-based aircraft configuration[30]. For this aircraft, changes in when the freeze of the transition model was invoked saw little change in the final flow solution. However, computational study of a S207-based wind tunnel model using the AFT2 model, which will be more thoroughly described in Section V, saw a slow transient that pushed the transition line further upstream on the surface of the wing over the course of several thousand cycles. This encouraged a revisit of two-dimensional results, and a third simulation was completed, denoted Run 3. Run 3 used Run 2 as its initial condition and was run at the same flow conditions of a Mach number of 0.7, a Reynolds number of 13.2 million, an α of -1.3° , and a Tu_∞ of 0.07% ($N_{crit} = 9.0$). The transition prediction model was unfrozen for the first 2000 cycles, and then frozen for a remaining 8000 cycles. The C_L computed by Run 3 was 0.652, and the C_D was predicted to be 0.0039. These force coefficients are again in close proximity to the MSES design report results. Note that of Run 1, Run 2, and Run 3, Run 3 has the highest C_D value.

Table 1 more compactly summarizes Run 1, Run 2, and Run 3, and Figure 7 shows the C_L and C_D computed from these simulations plotted against the polar included in the S207 airfoil design report[8]. Each one of the simulations predicted a point that fell slightly lower than the upper limit of the low-drag bucket, and computed C_D values that are 4 to 13 counts higher. The solution histories for each of the three simulations are included in Figure 8. Significant oscillations are observed when the transition equations are allowed to evolve. Even in the case of Run 3, which used an already sufficiently converged solution as its initial condition, difficulty was encountered in decreasing the density residual when transition was unfrozen. Furthermore, application of the transition freeze at 3250 cycles is sufficient for Run 1, as the C_L value appears to be relatively constant at this point in the simulation. However, this is not the case for Run 2, as the C_L appears to be changing significantly still at 3250 cycles. This is further shown by the restart in Run 3. Figure 9 shows a comparison between the surface C_f values for the fore and aft elements for Run 1, Run 2, and Run 3. Note that negative C_f is plotted on the lower surface of both elements. The S207 airfoil design report emphasizes that the transition from laminar to turbulent flow occurs at approximately 87% of the chord length on the upper surface of the aft element and that there exists a laminar separation bubble near the trailing-edge of the fore element[8]. All three simulations, Run 1, Run 2, and Run 3, are successful in predicting transition on the upper surface of the aft element, as this is where a large increase in C_f is observed. Run 1 and Run 3 predict transition to occur at 88% the chord length, whereas, Run 2 predicts a slightly more upstream location at 84% the chord length. The presence of the laminar separation bubble is evident on the fore element profile of all three runs as the C_f value changes in sign

near the trailing-edge on the upper surface. A large deviation from design metrics is observed in Run 3 as transition is predicted to occur on the lower surface of the fore element at the entrance of the slot. This suggests once again that the Run 2 solution was not sufficiently converged before the transition freeze was applied at 3250 cycles.

Table 1 NSU2D S207 Airfoil Simulation Summary at Mach = 0.7, $Re=13.2 \times 10^6$, and $\alpha=-1.3^\circ$

Simulation	Modeling	Cycles	Tu_∞	Trans. Freeze	Initial Condition	C_L	C_D
Run A	SA	100	NA	NA	Freestream	NA	NA
Run 1	SA-AFT2	10000	0.001%	3250	Run A	0.658	0.0032
Run 2	SA-AFT2	20000	0.07%	3250	Run A	0.620	0.0035
Run 3	SA-AFT2	10000	0.07%	2000	Run 2	0.652	0.0039

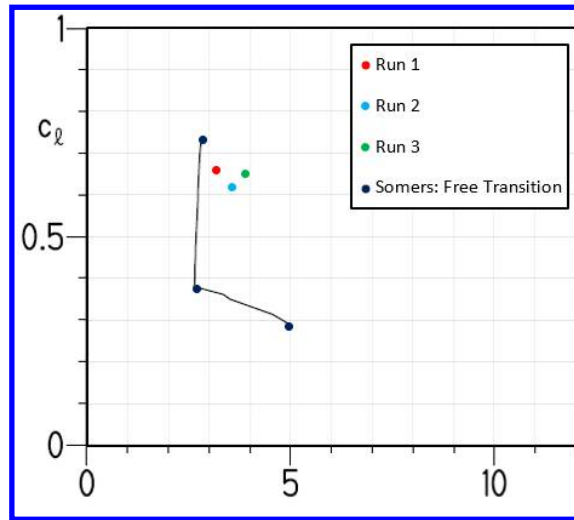


Fig. 7 NSU2D-AFT2-SA Simulation Results Compared to MSES Results Presented in Reference[8] for Mach = 0.700, $Re = 13.2 \times 10^6$, $\alpha = -1.3^\circ$

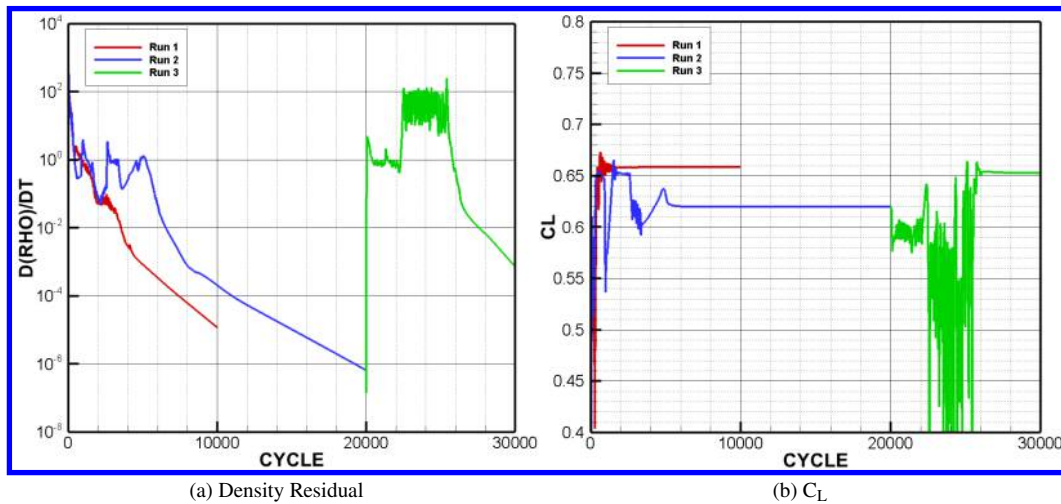


Fig. 8 NSU2D-AFT2-SA Solution Histories for Mach = 0.7, $Re = 13.2 \times 10^6$, and $\alpha = -1.3^\circ$

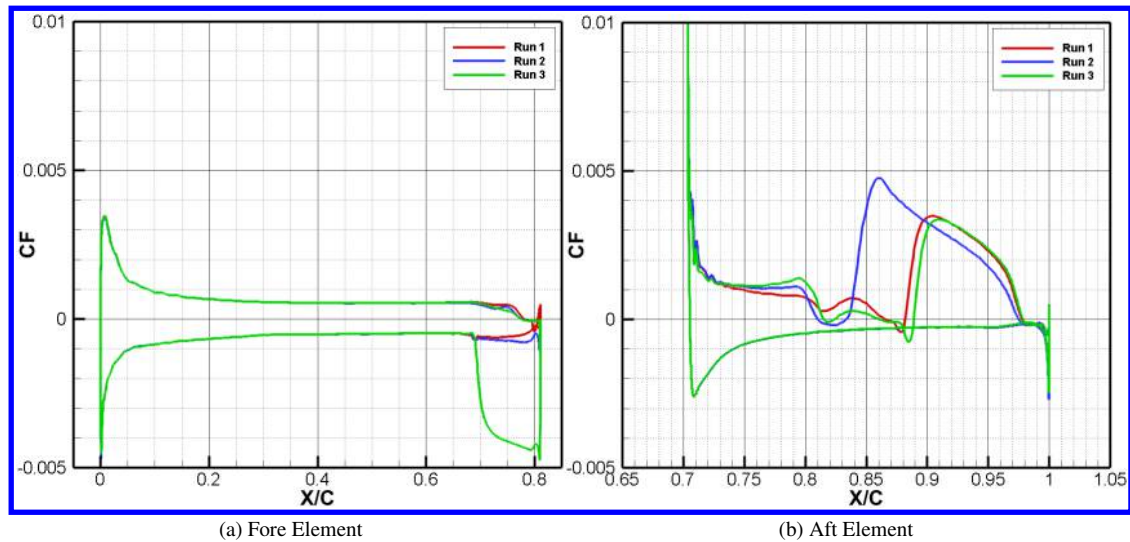


Fig. 9 NSU2D-AFT2-SA C_f Solutions for Mach = 0.7, $Re = 13.2 \times 10^6$, and $\alpha = -1.3^\circ$

B. Effect of Varying Tu_∞

The previous results indicate the presence of a slow solution transient in the NSU2D solutions for S207 airfoil calculations that tends to move the transition line further forward for a Mach number of 0.7, a Reynolds number of 13.2 million, an α of -1.3° , and a Tu_∞ of 0.07% ($N_{crit} = 9.0$). To determine how far forward the transition line is pushed by this transient on the S207 airfoil, Run 2 was rerun for 15000 cycles without use of the freeze of the transition prediction model. The surface C_f profile for this simulation is shown in Figure 10. This solution shows even more deviation from the MSES generated results in the S207 airfoil design report than Run 3. Not only is transition predicted on the lower surface of the fore element in the region of the slot, but also on the upper surface of the fore element at 35% the chord length.

Due to the slow transient and poor convergence behavior observed in two-dimensional S207 airfoil results for a Tu_∞ of 0.07% ($N_{crit} = 9.0$), an investigation was conducted to evaluate the effect of Tu_∞ on the overall low-drag bucket results compared to MSES. Several performance polars were developed for the S207 airfoil using NSU2D for Mach numbers of 0.700 and 0.650, a Reynolds number of 13.2 million, and varying values of Tu_∞ . All simulations were run for 15000 cycles to ensure a stationary or near stationary transition line. Results are shown in Figure 11 and indicate Tu_∞ values in the realm of 0.02% ($N_{crit} = 12.0$) and 0.04% ($N_{crit} = 10.34$) most closely align with MSES results, which again used a Tu_∞ of 0.07% ($N_{crit} = 9.0$).

IV. Effect of Transition in Three Dimensions

Three-dimensional computational analysis in support of the ULI was concerned with a S207-based SNLF TTBW aircraft that is based on the 2015 version of the Boeing SUGAR aircraft[33]. The wing of the SNLF TTBW vehicle was resized from 1477ft² to 1350ft² to account for the higher maximum C_L of the clean S207 airfoil[15, 34]. The 19.56 aspect ratio[13, 15, 33] and 12.5° of sweep[13, 33] were maintained. The twist is defined as two degrees of linear washout on the inboard panel and an additional degree in the outboard panel. A three-view of the aircraft is shown in Figure 12 and does not include the strut, as it was not considered in the current aerodynamic analysis. Three versions of a half-span model of the S207 SNLF TTBW configuration were analyzed computationally, with the grid for each being generated using the Pointwise software by ULI collaborators at the University of Tennessee at Knoxville. The Menter model was used for the first two versions of this aircraft, and associated results can be viewed in reference[16]. Only results for the final configuration, being acquired almost exclusively with the AFT2 transition prediction model, will be included in this paper. The grid generated for this configuration has 72 million points and is hybrid, with prisms in the near-wall boundary layer regions and tetrahedral elements in the regions of inviscid flow. Images of the grid can be viewed in Figure 13.

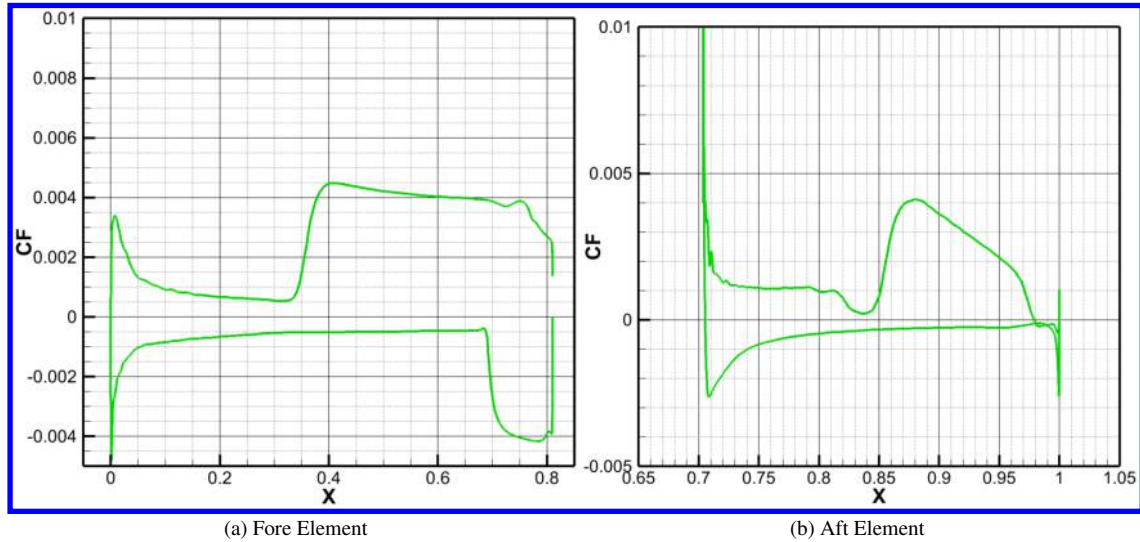


Fig. 10 NSU2D-AFT2-SA C_f Solution for Mach = 0.7, $Re = 13.2 \times 10^6$, $\alpha = -1.3^\circ$, and $Tu_\infty = 0.07\%$ ($N_{crit} = 9.0$) Run for 15000 Cycles with no Transition Freeze

A. The Menter Model vs. The AFT2 Model

A test case was run for the S207-based SNLF TTBW configuration to evaluate the behavior of the transition prediction line on the surface of the S207-based wing. The single-equation Menter model was used and the flow parameters for this test case are a Mach number of 0.7, a mean aerodynamic chord-based (MAC-based) Reynolds number of 12.3 million, an α of -1.0° , and an N_{crit} of 8.4 ($Tu_\infty = 0.09\%$). Due to the poor convergence that was observed in two-dimensional results that affects the location of the transition line, this three-dimensional case was run for 15000 cycles to ensure a stationary transition line. The upper surface C_f for this test run can be viewed in Figure 14a. Note that these results show a transition line that is very undesirable and is in disagreement with the design intent of the S207 airfoil as the turbulent regime begins at the leading-edge on the inboard panel of the wing. An additional simulation was run using the AFT2 model at a Mach number of 0.7, an MAC-based Reynolds number of 12.3 million, an α of -1.0° , and an N_{crit} of 8.4 ($Tu_\infty = 0.09\%$). The upper surface C_f profile is shown in Figure 14b. These results are much more in line with the design intent of the S207 airfoil as the upper surface of the fore element appears to be entirely laminar. This suggests that the AFT2 model is more suited to accurately predict the performance of the S207 airfoil and that the Menter model may be limited by high Reynolds numbers.

B. Effect of Varying Transition Prediction Surface Application

Though the AFT2 model predicts improved laminar flow behavior on the surface of an S207-based wing, further adjustment to the approach was still necessary. Note that in Figure 14b the nose of the aircraft is blue, an indication of laminar flow. This is an unrealistic prediction as laminar flow should not be present on the fuselage[33]. It was at this point in the analysis that the patch-based and box-based transition model application capabilities of NSU3D discussed in Section II.C were implemented and utilized. Note that the solution depicted in Figure 14a was acquired using this capability.

Two drag polars, both requested by ULI project members at the Boeing Company and referred to as Cases 1 and 2 from here on in, were developed using the final configuration of the S207-based SNLF TTBW aircraft for a Mach number of 0.7273, a MAC-based Reynolds number of 12.3 million, and an N_{crit} of 8.4 ($Tu_\infty = 0.09\%$). The α was constrained to values ranging from -1° to 2.5° . Each case applied the transition model to only regions of the wing, excluding the fuselage. Case 1 modeled the entire wing as free transition. Case 2 is representative of leading-edge tripping, with the lower surface of the fore element being modeled as fully turbulent starting at 3% chord to simulate the presence of a stowed Krueger flap. A segmented profile of the S207 airfoil cross section as well as a table specifying free transition application for Cases 1 and 2 is shown in Figure 15. C_L and C_D values computed by each of the simulations conducted as part of Cases 1 and 2 are compared in Figure 16a, Figure 16b, and Table 2. Furthermore, the computed C_f values are plotted as a function of α in Figure 16c for Cases 1 and 2. The formation of a low-drag bucket can be

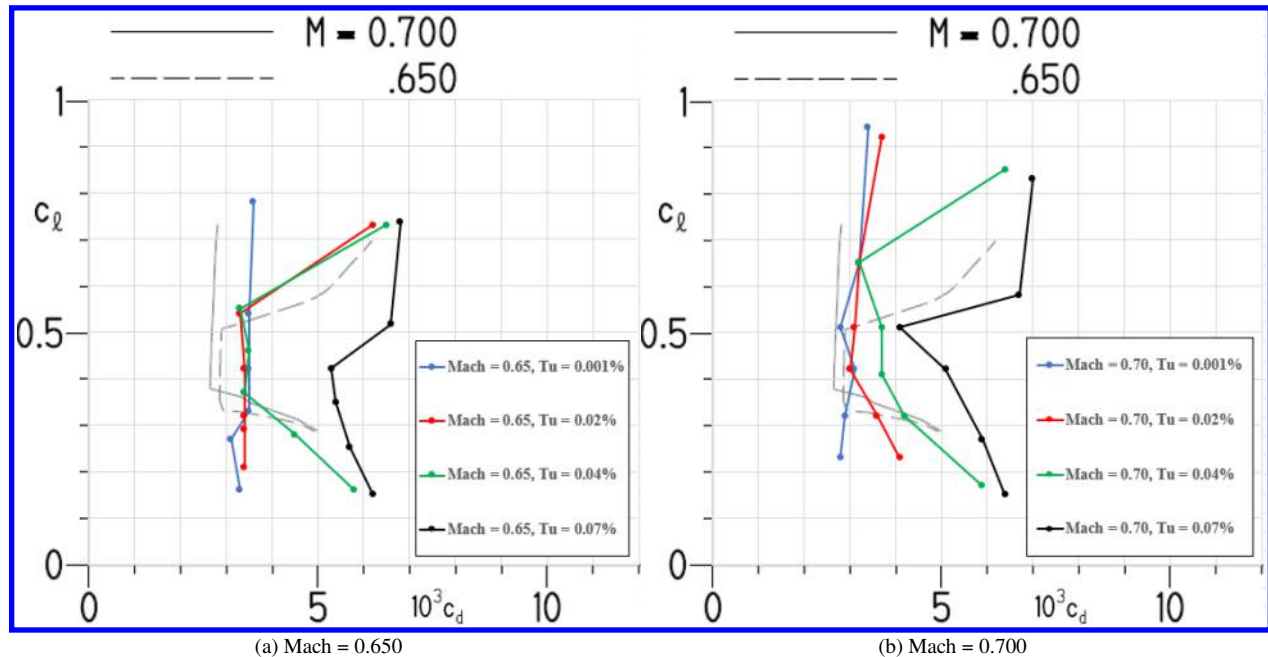


Fig. 11 NSU2D-AFT2-SA Performance Polars for $Re = 13.2 \times 10^6$ Run for 15000 Cycles with no Transition Freeze

observed between the α values of -1.5° and 0.5° . Unsurprisingly, Case 1 predicts higher C_L values and lower C_D values for all angles of attack. This is due to the modeled runs of laminar flow on the lower surface of the fore element for Case 1 simulations. The upper surface C_f contours for Case 1 simulations are shown in Figure 17a, and the same is done for the lower surface in Figure 17b. From these images it can be stated that laminar flow is more significant on the upper surface for lower angles of attack, and the opposite is true for the lower surface. Additionally, this shows that the transition prediction model is behaving as expected with variations in α .

Table 2 NSU3D-AFT2-SA Free Transition Lift and Drag Values for S207-Based SNLF TTBW Aircraft at Mach = 0.7273, $Re_{MAC} = 12.3 \times 10^6$, $N_{crit} = 8.4$ ($Tu_\infty = 0.09\%$)

Case Number	Angle of Attack	C_L	C_D
Case 1: Free transition on upper/lower surfaces of wing	-2.00°	0.0250755809	0.0206113068
	-1.00°	0.2519359000	0.0194720149
	0.00°	0.4332683130	0.0210144158
	1.00°	0.6000374260	0.0251781831
	1.50°	0.6864091240	0.0274875215
	2.00°	0.7750443420	0.0301037591
	2.50°	0.8651606570	0.0331735695
Case 2: Free transition on upper surface of wing/ Tripped 3% chord on lower surface of wing	-2.00°	-0.0087226616	0.0210632758
	-1.00°	0.2192064180	0.0205394374
	0.00°	0.4074759850	0.0224077157
	1.00°	0.5677787590	0.0263974269
	1.50°	0.6571697780	0.0285320763
	2.00°	0.7479776920	0.0309886014
	2.50°	0.8381463260	0.0339210770

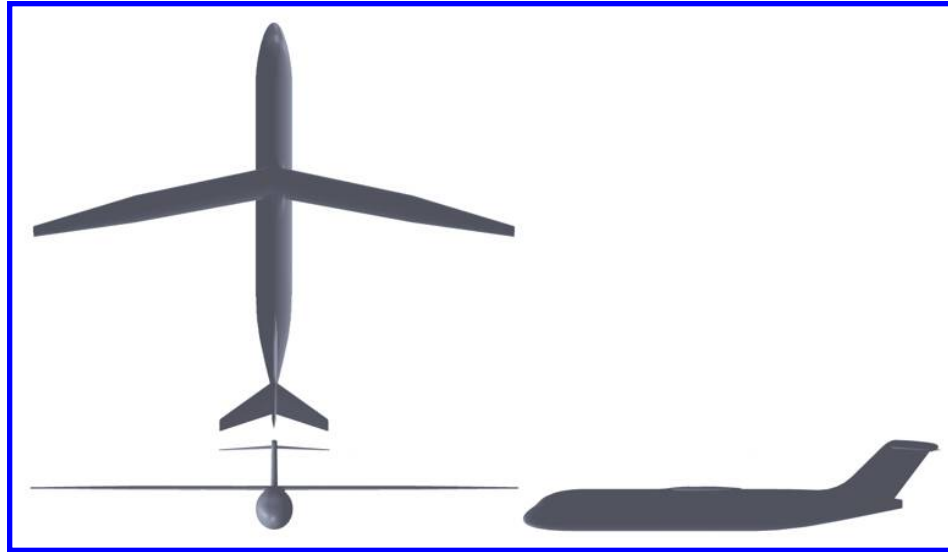


Fig. 12 S207-Based Slotted, Natural-Laminar-Flow Transonic Truss-Braced Wing ULI Aircraft

A final investigation was undertaken as part of the surface-based transition prediction application efforts conducted on the S207-based SNLF TTBW aircraft to determine if the transition on the upper surface of the wing would be impacted by a reduction in turbulent flow near the fairing. It is worth noting that flow separation at the wing-fairing junction has been observed on this aircraft, indicating a poorly designed wing-fairing junction. Three simulations at a Mach number of 0.7273, an angle of attack of 1° , and a Reynolds number of 12.3 million were performed, each with a progressively larger region of application of the free transition model at the wing-fairing junction. This is illustrated in Figure 18. The predicted upper surface C_f profiles are catalogued in Figure 19. From these results, the location of the wing upper surface transition line does not seem to be significantly impacted by the application of the transition model in the region of the wing-fairing junction on this computational model.

C. Performance Polars for the S207-Based SNLF TTBW Aircraft

In addition to a strictly fully turbulent approach, the modeling strategies employed for Cases 1 and 2 were further utilized to generate full performance polars. Fully turbulent drag polars and drag polars where free transition was applied to the entire wing (Case 1 specifics) were run for Mach numbers ranging from 0.200 to 0.750. Values of α were incremented from -2° to 5° . The polars developed by applying free transition modeling to the entire wing except for the lower surface of the fore element (Case 2 specifics) required a reduction in cases due to lack of computational resources. The upper and lower limit of Mach numbers used were adjusted to 0.400 and 0.730, with every other Mach number typically used being omitted. Additionally, α values were instead only incremented from -1° to 3° . MAC-based Reynolds number was 12.3 million and in the case of free transition modeling an N_{crit} of 8.4 ($Tu_\infty = 0.09\%$) was used. This data was requested and provided to ULI associates at The Boeing Company for use in their analysis of the S207-based SNLF TTBW aircraft[35].

C_L and C_D curves for the fully turbulent simulations are shown in Figure 20, and drag polars are shown in Figure 21. Pitching moment curves are included as Figure 22, and both pressure drag and C_f are quantified in Figure 23. Note that the C_f profile is relatively constant for each Mach number as expected for fully turbulent cases.

The C_L and C_D curves associated with data generated by applying free transition modeling to the entire wing are viewable in Figure 24. The drag polars are shown in Figure 25a, and these drag polars for Mach numbers of 0.5 and 0.7 are compared to the corresponding fully turbulent curves in Figure 25b. More beneficial behavior is observed with the application of a transition prediction model as was demonstrated in two dimensions. The pitching moment curves and drag curves are included as Figure 26 and Figure 27, respectively. Figure 27a predicts the formation of a low-drag bucket between -1° and 2° , which can be compared to Figure 23a which shows no formation of a low-drag bucket for fully turbulent simulations.

To establish correspondence between two-dimensional and three-dimensional results, comparisons between two-dimensional and three-dimensional fully turbulent pressure profiles were made as well as comparisons between spanwise

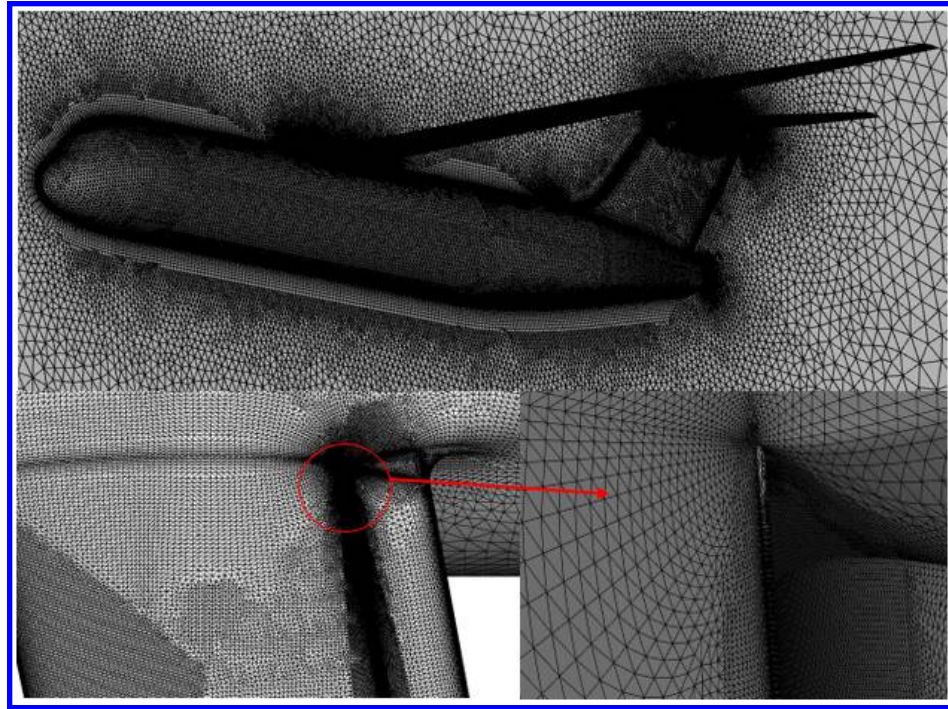


Fig. 13 Grid Generated for the S207-Based SNLF TTBW Aircraft Configuration

C_L values and MSES computed low-drag bucket C_L conditions. The spanwise MAC-based and local chord-based C_L values found with free transition modeling applied to the entire wing (Case 1 specifics) are plotted for Mach numbers of 0.5 and 0.7 in Figure 28. Most of the spanwise C_L values based on local chord for a Mach number of 0.7 and angle of attack of 0° successfully fall between the upper and lower limits of the low-drag bucket as defined in the design report of the S207 airfoil[8]. Fully turbulent C_p profiles for two- and three-dimensional simulations at a Mach number of 0.7 are shown in Figure 29. These profiles do not include sweep corrections which would be on the order of 5% for the wing sweep of 12.5° . The station nearest the fuselage shows poor agreement with two-dimensional predictions. The outboard stations show better agreement but the C_p values on the upper and lower surfaces are closer together than what is predicted by two-dimensional results, so less lift is generated in comparison. The pressure at the trailing edge of the fore element, however, is computed to be less adverse than what is predicted by two-dimensional results.

The lift and drag curves for the polars developed by limiting the regions of free transition to the upper surface of the fore element, the first 3% of the lower surface of the fore element, and the entirety of the aft element are shown in Figure 30. Drag polar curves are shown in Figure 31, and C_f and pressure drag curves are shown in Figure 32. Note that in Figure 30b the Mach=0.4 and Mach=0.5 curves cross over each other at an angle of attack of 0° . This behavior is even more pronounced in Figure 32a. C_f contours for these two cases are shown in Figure 33. There is more laminar flow predicted to occur at a Mach number of 0.5 than there is at a Mach number of 0.4 when the angle of attack is 0° which results in less drag at this higher Mach number. The same comparison was made for the previous polar set in which free transition was applied to the entire wing, as shown in Figure 34. Similar behavior is observed. The pressure gradient along the upper surface is expected to become less favorable as Mach number decreases[8], so the weaker suction peaks and weaker compressibility effects are likely the cause of this observed cross over between results for Mach numbers of 0.4 and 0.5.

D. Additional 3D Free Transition Investigation for a S207-Based SNLF TTBW Aircraft

Section III.B describes an investigation conducted to study the location of the transition line on the S207 airfoil as it relates to the freestream turbulence intensity Tu_∞ . Tu_∞ values of 0.02% ($N_{crit}=12.0$) to 0.04% ($N_{crit}=10.34$) were found to be most successful in establishing correspondence between NSU2D CFD solutions and original design values acquired using MSES[8]. In this section, the effect of Tu_∞ values on performance prediction is expanded to three dimensions via the development of a single polar at a Mach number of 0.7273, a MAC-based Reynolds number of

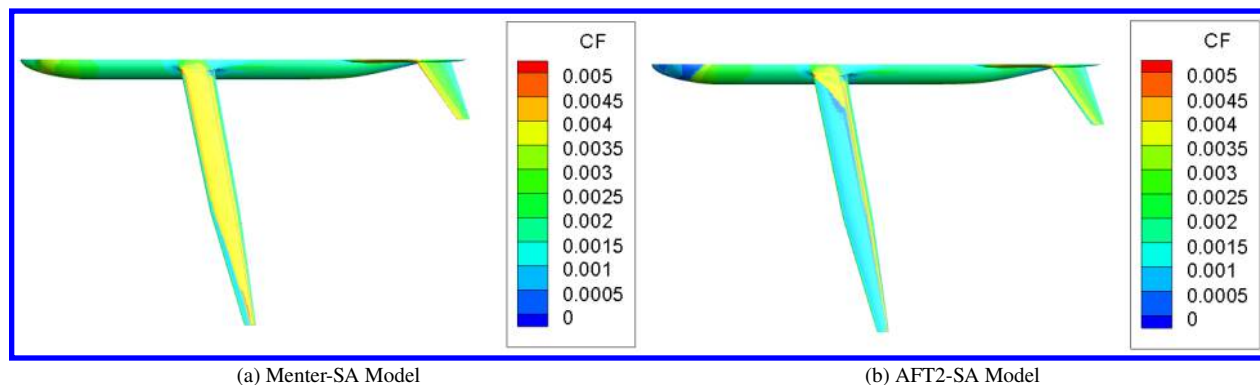


Fig. 14 NSU3D Generated Upper Surface C_f Contours at Mach = 0.7, $Re_{MAC} = 12.3 \times 10^6$, $\alpha = -1.0^\circ$, and $N_{crit} = 8.4$ ($Tu_\infty = 0.09\%$) for the S207-Based SNLF TTBW Configuration

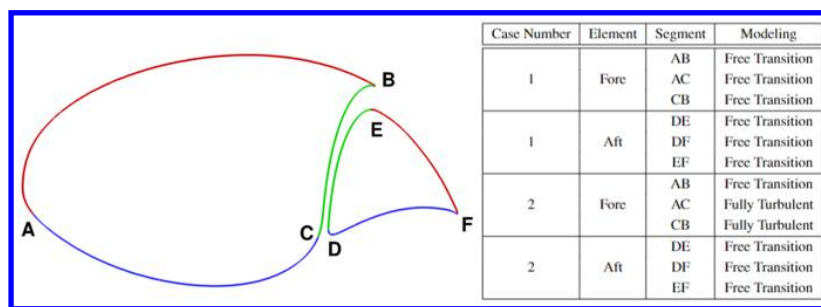


Fig. 15 Division of S207 Profile for Flow Model Application with Application Specifications for Cases 1 and 2

12.3 million, and a N_{crit} value of 10.4 ($Tu_\infty = 0.039\%$). Note that this N_{crit} value is associated with a Tu_∞ value that is slightly lower than 0.04%, but the difference is small and not expected to significantly impact results. The upper and lower surface C_f contours for these polar simulations are included in Figure 35 and Figure 36, respectively. These solutions show laminar flow on the nose of the aircraft as the transition prediction model was applied to the entire body. However, it can be assumed the presence of this laminar flow on the nose does not impact the flow regime on the wing given the results from the study associated with Figure 18 and described in Section IV.C. Comparing the results for a N_{crit} value of 10.4 to Figure 17 offers evidence that expected trends with changes in N_{crit} (or Tu_∞) are held over the entire drag polar range for the investigated flow conditions, with the transition line being consistently predicted to occur further downstream on both the upper and lower surface for the lower Tu_∞ simulations.

V. Computational Results for a S207-Based Wind Tunnel Model

A. The NASA Ames Wind Tunnel Tests

Efforts conducted under the NASA ULI to thoroughly establish the benefits of SNLF technology and set forth the S207 airfoil as a superior foundation for commercial aircraft included a capstone demonstration performed in the NASA Ames UWPT 11-ft transonic wind tunnel in February and March of 2022. A main consideration of the experimental campaign was to determine if desired regions of natural laminar flow could be maintained on an S207-based model with moderate sweep and the necessary bracketing hardware to connect the fore and aft element. The sweep of this S207-based model was 12.5° , and the chord was a constant 2ft. Three connectors attached the aft element to the fore element and enabled aft element repositioning for high-lift configurations. Three rows of pressure ports were installed at inboard, midboard, and outboard locations. A diagram summarizing the construction of the model can be viewed in Figure 37a. The completed installation in the wind tunnel is included as Figure 37b.

The model was painted matte black in anticipation of infrared (IR) thermography analysis. Figure 38a shows an image acquired using this methodology visualizing the flow on the upper surface near the fairing at a Mach number of

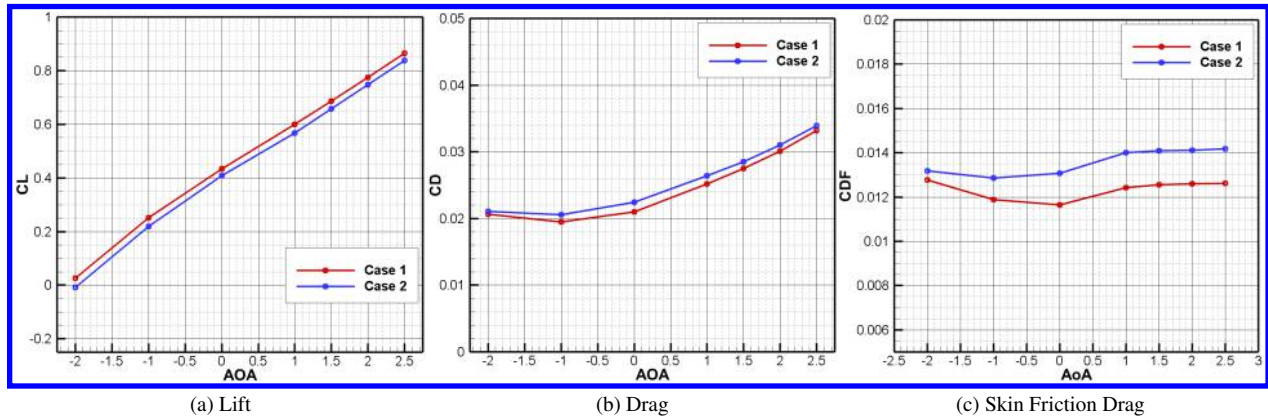


Fig. 16 NSU3D-AFT2-SA Free Transition Force Coefficient Curves at Mach = 0.7273, $Re_{MAC} = 12.3 \times 10^6$, and $N_{crit} = 8.4$ ($Tu_{\infty} = 0.09\%$) for the S207-Based SNLF TTBW Aircraft

0.699, an angle of attack of -0.002° , and a Reynolds number of 12.93 million. Similarly, Figure 38b shows the flow at this location for a Mach number of 0.701, an angle of attack of -1.000° , and a Reynolds number of 12.95 million. Distinct transition lines produced by the pressure port rows are observed in Figure 38b. In comparison, Figure 38a shows no indication of transition, suggesting that laminar flow is present for the entirety of the upper surface of the wing at these flow conditions. These results confirm that the configuration produces large regions of natural laminar flow and thus behaves as intended according to design. Additionally, results suggest that any cross flow instabilities resulting from the 12.5° of sweep are not significant enough to induce transition for angles of attack of 0° and -1° .

B. Wind Tunnel Model Grid

The wind tunnel campaign was supported with CFD simulations completed on a wind tunnel model representative of the experimental setup. The grid was generated by collaborators at the University of Tennessee at Knoxville using the Pointwise software. The mesh is unstructured with 168,877,277 nodes, and it is hybrid with prisms in the near-wall boundary layer and pyramids and tetrahedral elements in the regions of inviscid flow. The mesh of the wing-fairing structure is shown in Figure 39 and is accompanied by additional images of the wing-fairing junction to emphasize the refinement through the slot.

The wing-fairing structure is placed in a channel 84.7 chord lengths from inlet to outlet. The inlet and outlet are square being 5.36 chord lengths in width and length. The nose of the fairing is a distance of 5.33 chord lengths from the inlet. Diagrams of the full channel are shown in Figure 40.

C. Results for $N_{crit} = 8.4$

The first simulation performed using the wind tunnel model grid utilized a fully turbulent approach. This was done to both establish a successful run prior to introducing the complexities associated with transition prediction, and to gain insight on the computational requirements for this grid, given its size. This simulation was run at a Mach number of 0.7, an angle of attack of 0° , and a Reynolds number of 12 million. The CL and CD values were computed to be 0.3611 and 0.0335, respectively. The convergence history over 10000 cycles for CL and the density residual are shown in Figure 41.

In anticipation of the increased computational demands associated with the transition prediction model and to ensure that adjusting the CFL number would not drastically impact the transition location when utilizing a free transition model, a numerical effort was undertaken in which three free transition simulations, using the AFT2 model, were completed with varying CFL numbers. These simulations are denoted as Simulation 1, Simulation 2, and Simulation 3. It became clear immediately following initial runs that a solution started from uniform freestream conditions would numerically diverge if the CFL number was set to a value greater than 2. The decision was made to run a single free transition simulation for 10000 cycles using a CFL number of 2 that would then be used to start the three desired solutions with varying CFL numbers. This simulation is denoted as Baseline. All solutions, Simulations 1, 2, 3, and Baseline, used an N_{crit} value of 8.4 ($Tu_{\infty} = 0.09\%$). No longer being started from a uniform freestream solution, the CFL number for Simulation 1 was set to 10 and the CFL number for Simulation 2 was set to 25. Both of these cases were run for an

additional 10000 cycles. Simulation 3 experienced no increase in CFL number and was instead run for another 32000 iterations at a CFL number of 2. Table 3 more compactly summarizes each case and their specifications along with corresponding computed force coefficient values. Figure 42 shows the CL and density residual convergence histories. It should be noted that the residuals in NSU3D are scaled by the CFL number, so the increase in the density residuals observed for Simulations 1 and 2 in Figure 42b does not indicate undesirable convergence. However, the residual for Simulation 2 increases over 5000 cycles which is not ideal or desirable, and running for longer than 10000 additional cycles defeated the purpose of the cost reduction benefits expected with the increase in CFL.

Each of the three simulations computed roughly the same C_L value of ≈ 0.32 . This is an indication that altering the CFL number does not significantly impact the final solution values. To further support this claim and to investigate the behavior of the transition line as each simulation evolved, C_f contours were made at various stages of each solution. Figure 43 shows the upper and lower C_f profiles at the end of the Baseline simulation. In this case, both the upper and lower surface show laminar flow along the entire chord length of the wing with some turbulence near the fuselage and wingtip. C_f contours for the upper and lower surface of the wing at the end of Simulation 1 and Simulation 2 are shown in Figure 44 and Figure 45, respectively. Simulation 3 C_f contours were made for solutions at 18000 cycles (28000 total if including Baseline) and at the end cycle of 32000 (42000 total if including Baseline). These are shown for the upper and lower surfaces in Figure 46.

Table 3 NSU3D-AFT2-SA Wind Tunnel Model Simulations Performed at Mach = 0.7, $\alpha = 0^\circ$, Re = 12×10^6 , and $N_{crit} = 8.4$ ($Tu_\infty = 0.09\%$)

Case	CFL	Initial Condition	Total Cycles	CL	CD
Baseline	2	Freestream	10000	0.4260	0.02947
Simulation 1	10	Baseline	10000	0.3230	0.02715
Simulation 2	25	Baseline	10000	0.3214	0.02731
Simulation 3	2	Baseline	32000	0.3254	0.02696

Simulations 1, 2, and 3 show that the transition line moves, albeit very slowly, toward the leading-edge of the fore element as the solution converges. These simulations also predict the transition line to become stationary at approximately 40% the chord length, demonstrating that the steady-state transition line is predicted at roughly the same location by all runs with different CFL values, provided these cases are run for sufficient number of cycles. These results depict much more significant regions of turbulent flow in comparison to wind tunnel data.

D. Results for $N_{crit} = 6.0$

Following the delivery of results presented in the previous section to the ULI team at the University of Tennessee at Knoxville, a request was made for an additional simulation with an N_{crit} value of 6 ($Tu_\infty = 0.245\%$). This value was chosen to more accurately represent expected wind tunnel freestream turbulence conditions. This simulation was run at a Mach number of 0.7, a Reynolds number of 12 million, and an α of 0° . The CFL number was held at 2 to ensure the residuals did not begin to increase as was observed with Simulation 2, and 30000 cycles were executed. The convergence history for C_L and the density residual are shown in Figure 47. The C_L is computed to be 0.326 which is approximately equal to the value predicted by Simulations 1, 2, and 3, whose N_{crit} value was 8.4 ($Tu_\infty = 0.09\%$).

C_f contours were once again generated for various cycle numbers to evaluate the behavior of the transition line. Contours for the upper and lower surfaces are shown at 10000 cycles, 20000 cycles, and 30000 cycles in Figure 48. These C_f contours show that when N_{crit} is set to 6 the transition line begins at the trailing-edge of the fore element and moves toward the leading-edge, stopping at about 40% of the chord length, as the solution converged. This is similar to the behavior observed with Simulations 1, 2, and 3, but again is in disagreement with the extensive runs of laminar flow observed in the NASA Ames wind tunnel tests for these flow conditions.

To investigate the discrepancies between computational and experimental results further, surface pressure profiles collected at the three experimental pressure port row locations, as shown in Figure 37a, were compared to computational results. These pressure port row locations are denoted as L1 for the inboard location, L2 for the midboard location, and L3 for the outboard location. Data for two wind tunnel tests at approximately a Mach number of 0.7, a Reynolds number of approximately 13 million, and an α of roughly 0° were available for examination. They are denoted as Run 204 and Run 297, and their exact flow parameters are summarized in Table 4. Surface pressure data was post-processed and

provided by ULI associates at Texas A&M University. Figure 49 illustrates the C_p profiles for both Run 204 and Run 297 plotted against the C_p profiles of the $N_{crit} = 6$ ($Tu_\infty = 0.245\%$) solution at 10000 cycles and 30000 cycles. Figure 50 shows surface pressure contours across the upper and lower surfaces for the CFD solution at 10000 cycles and 30000 cycles appended with lines associated with the pressure port row locations.

Table 4 Flow Parameters for Examined Wind Tunnel Runs

Run	Mach	Reynolds Number	Angle of Attack
204	0.7013	12.95 Million	-0.0001
297	0.6994	12.93 Million	-0.0002

Upon examination of Figure 49, it can be stated that the surface pressure profiles for the computational solution at 10000 cycles and 30000 cycles do not differ much with the exception of in the region of the slot and on the upper surface of the flap. Surprisingly, there are notable differences between the experimental runs. Run 297 has a lower, or more negative, pressure through the slot than Run 204 at all three locations. On the contrary, Run 204 has a lower pressure than Run 297 on the upper surface of the fore element at the trailing edge for all locations. This is also true on the upper surface of the aft element following the exit of the slot. Comparing the experimental and computational results, it is clear that the pressure on the upper surface of the fore element computed using CFD is lower across the entire surface at all three locations. Location L1 data shows that the computational results have a lower pressure through the slot. The opposite is true at locations L2 and L3, with experimental results having lower pressure through the slot. At the L3 outboard location, computational results agree well with Run 204, but not as well with Run 297. Additionally, the pressure profile on the upper surface at the trailing-edge of the aft element at the L3 location shows a pressure that is much lower than experimental results. It is relatively flat, indicating flow separation. Examination of Figure 50 offers evidence that this region of constant pressure starts just slightly outboard of the L2 pressure port row and continues just outboard of the L3 pressure port row. Similar regions of constant pressure are also observed at the trailing-edge near the fairing and at the trailing-edge of the wing tip. Large localized pressure variations, or spikes, are seen on the upper surface of the fore element at location L2. This was traced to the presence of a non-smooth surface on the computational geometry.

In summary, the computational results obtained in support of the wind tunnel tests conducted for a swept SNLF wing-fairing model showed several discrepancies. In particular, significantly more laminar flow was observed in the wind tunnel experiment than in the computational results. This may be due to the convergence difficulties that accompany the transition model used in the computational framework. There is also a possibility that discrepancies in the computational geometry are triggering transition earlier than desired. For example, the current geometry did not account for the additional thickness accompanied by the paint layer, and surface irregularities were noted on the computational geometry as discussed previously. Given the sensitivity of SNLF technology to geometry, it is possible this lack of consideration may negatively impact the computational performance of the model. Additionally, differences in the surface pressure profiles between Runs 204 and 297 suggest that there may be issues in the repeatability of the experiment, particularly at the slot where the flow is known to be very sensitive to geometry variations[16]. Furthermore, aeroelastic deformation was not taken into account in the CFD simulations, and there has been no assessment of what these deflections may be.

E. Results for $N_{crit} = 10.4$

Similar to the work described in Sections III.B and IV.D, the effect of freestream turbulence intensity Tu_∞ on the computed location of the transition line is further investigated through an additional simulation with the wind tunnel model. Using a N_{crit} value of 10.4, which corresponds to a Tu_∞ of 0.039%, saw closer agreement between CFD solutions for the S207-based TTBW vehicle and the S207 airfoil two-dimensional geometry with design intent[8]. This wind tunnel model simulation was run in an identical manner to the simulation described in the previous section, using up to 30,000 cycles to converge, with the only change being the adjustment in N_{crit} to 10.4 ($Tu_\infty = 0.039\%$). The density residual and lift coefficient convergence histories are compared to the $N_{crit} = 6.0$ ($Tu_\infty = 0.245\%$) simulation in Figure 51. The density residual decreases by the same order of magnitude despite the change in N_{crit} .

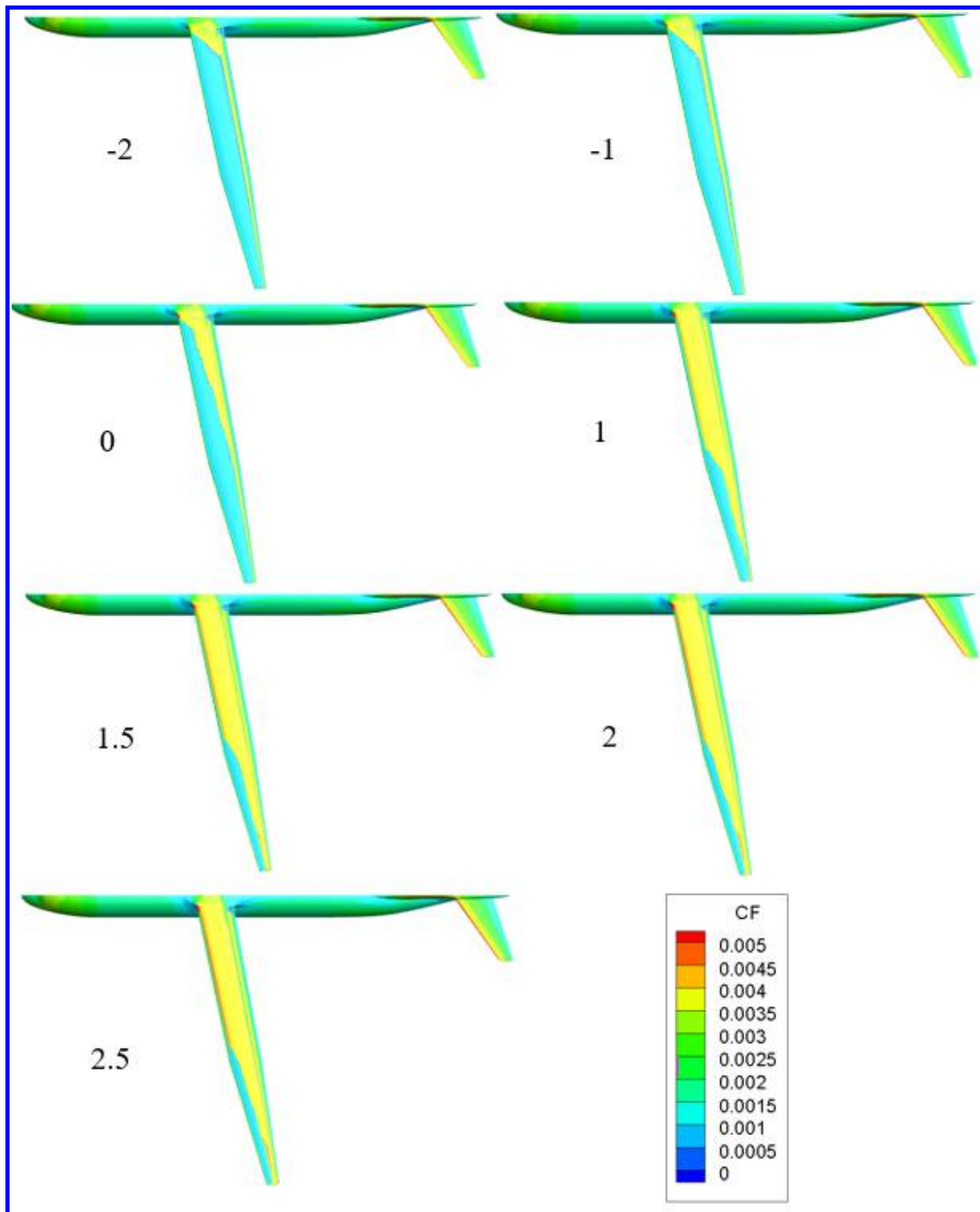
The upper and lower surface C_f contours for the wind tunnel solution in which $N_{crit} = 10.4$ ($Tu_\infty = 0.039\%$) is shown in Figure 52. In comparison to the $N_{crit} = 6.0$ ($Tu_\infty = 0.245\%$) simulation after 30000 iterations shown in Figure 48e and Figure 48f, there is much more laminar flow. The reduction in freestream turbulence intensity results in closer

agreement between NSU2D CFD solutions and original S207 airfoil design metrics, and in this case experimental results collected at NASA Ames. Although this lower Tu_∞ value is not representative of the wind tunnel experiment, these results confirm that consistent results are obtained between two-dimensional airfoil and three-dimensional full configuration results for these parameter settings.

VI. Conclusions

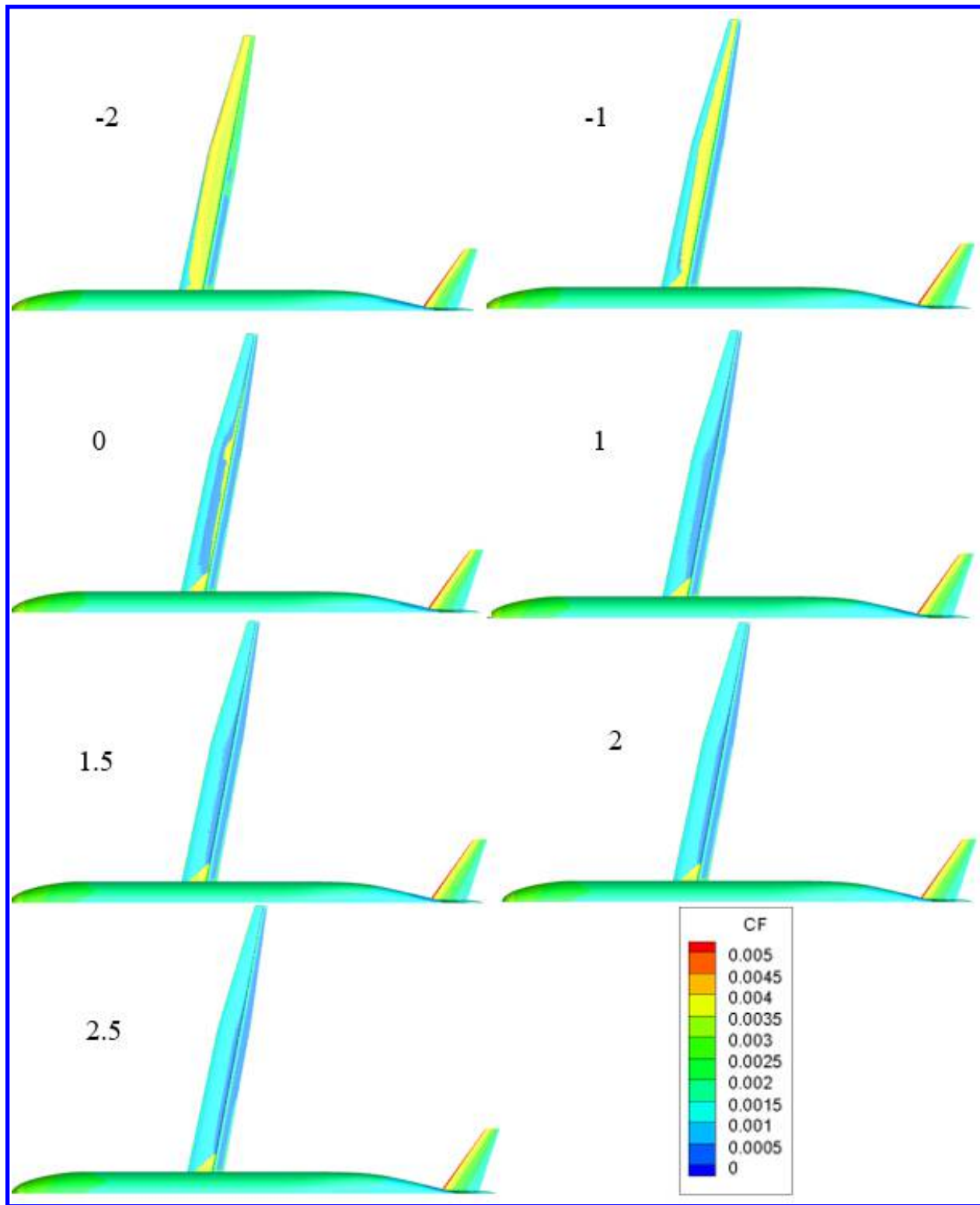
Computational fluid dynamics analyses of natural laminar flow configurations were carried out in this work in support of the design of an SNLF TTBW aircraft configuration based on the S207 SNLF airfoil, under a NASA University Leadership Initiative (ULI) project. After initial validation on two- and three-dimensional test cases, the free-transition RANS CFD methodology was used to analyze an SNLF TTBW aircraft configuration. Computations over an extensive set of flow conditions were used to produce drag polars for a range of Mach numbers, highlighting the differences between fully turbulent runs, free transitional runs, and free transitional runs on selected geometric components of the aircraft configuration. In general, the predicted trends of the transition behavior with Mach number, C_L or α , and Tu_∞ were consistent with expectations. Significant runs of laminar flow were observed for angles of attack ranging from -1° to 2° , which corresponds with the formation of a low-drag bucket observable through variation of the C_f values as a function of angle of attack. Spanwise C_L values based on local chord length fell within the upper and lower limits of the low-drag bucket for the S207 SNLF airfoil. However, comparison of fully turbulent sectional surface pressure profiles at select spanwise locations to two-dimensional turbulent surface pressure airfoil profiles revealed that there is some lack of agreement between two-dimensional and three-dimensional results, particularly through the slot. Three-dimensional effects likely play a role and further three-dimensional geometric modifications, or optimizations may be possible for improving the performance of swept SNLF-based wings.

Simulations conducted in support of wind tunnel experiments completed at NASA Ames resulted in several discrepancies between computational and experimental results. In the wind tunnel, laminar flow was observed on the entire upper surface of the wing at a Mach number of 0.699, Reynolds number of 12.93 million, and an angle of attack of -0.002° . Computational results predicted the transition from laminar to turbulent flow at approximately 40% chord length. These simulations revealed the presence of a slow transient during which the transition line moved forward during the solution convergence process. Improved agreement with experimental values was achieved by lowering the Tu_∞ levels used as input to the transition model based on two-dimensional results carried out for the S207 SNLF airfoil. While the overall trends in transition behavior were captured in the current study for a relatively complex SNLF TTBW configuration, improvements in convergence speed and robustness for free transition RANS models remain a pacing item for use in production.



(a) Upper Surface

Fig. 17 NSU3D-AFT2-SA Free Transition Case 1 C_f Contours at Mach = 0.7273, $Re_{MAC} = 12.3 \times 10^6$, and $N_{crit} = 8.4$ ($Tu_\infty = 0.09\%$) for the S207-Based SNLF TTBW Aircraft



(b) Lower Surface

Fig. 17 Cont. NSU3D-AFT2-SA Free Transition Case 1 C_f Contours at Mach = 0.7273, $Re_{MAC} = 12.3 \times 10^6$, and $N_{crit} = 8.4$ ($Tu_\infty = 0.09\%$) for the S207-Based SNLF TTBW Aircraft

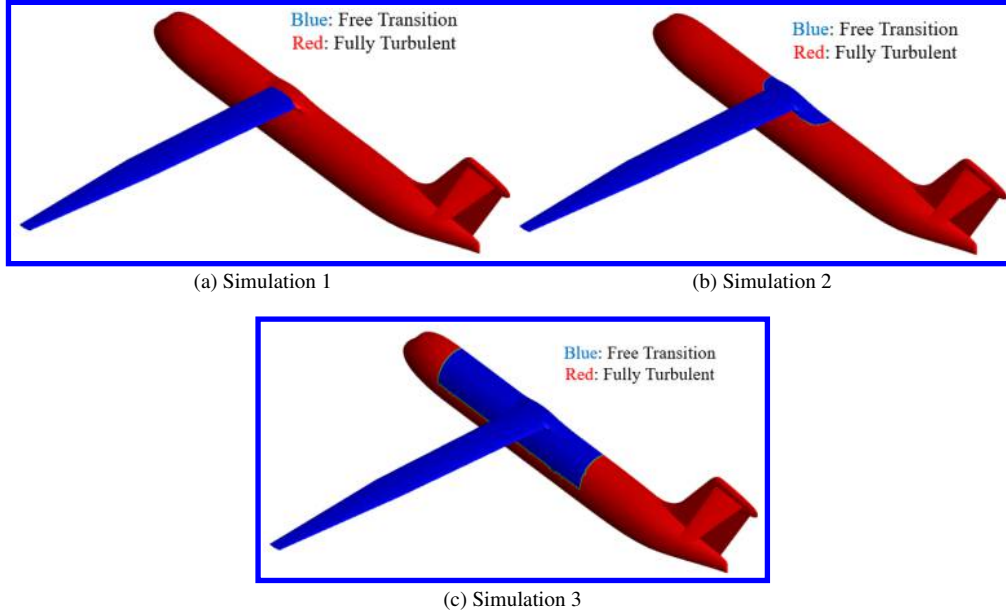


Fig. 18 NSU3D-AFT2-SA Free Transition Expansion Summary for the S207-Based SNLF TTBW Aircraft

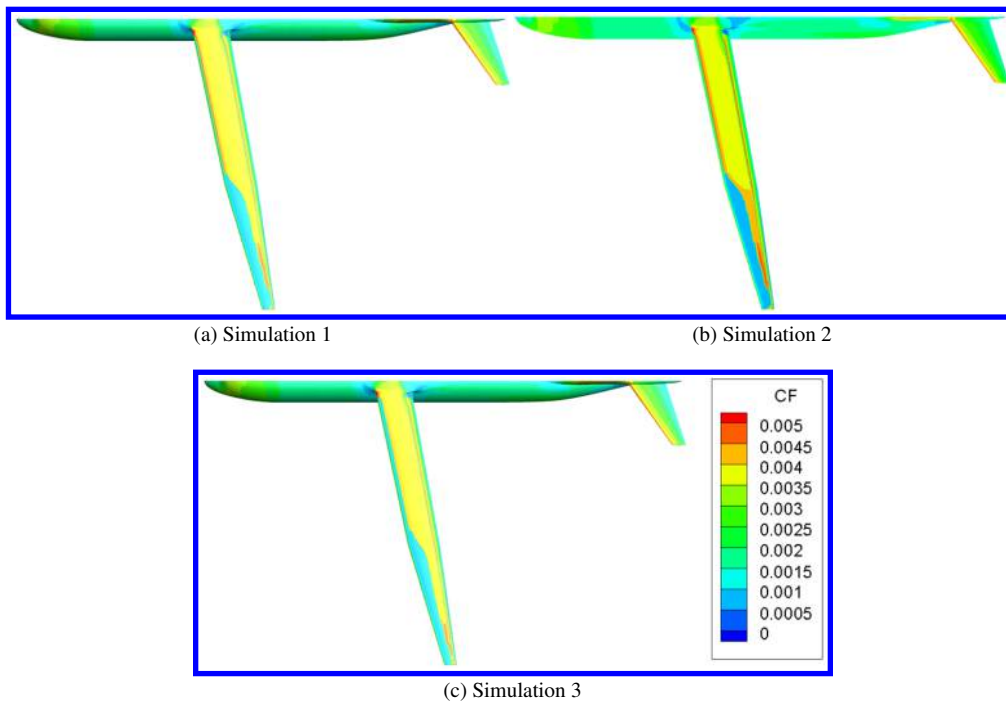


Fig. 19 NSU3D-AFT2-SA Free Transition Expansion Results at Mach=0.7, $Re_{MAC} = 12.3 \times 10^6$, $\alpha = 1^\circ$, and $N_{crit} = 8.4$ ($Tu_\infty = 0.09\%$) for the S207-Based SNLF TTBW Aircraft

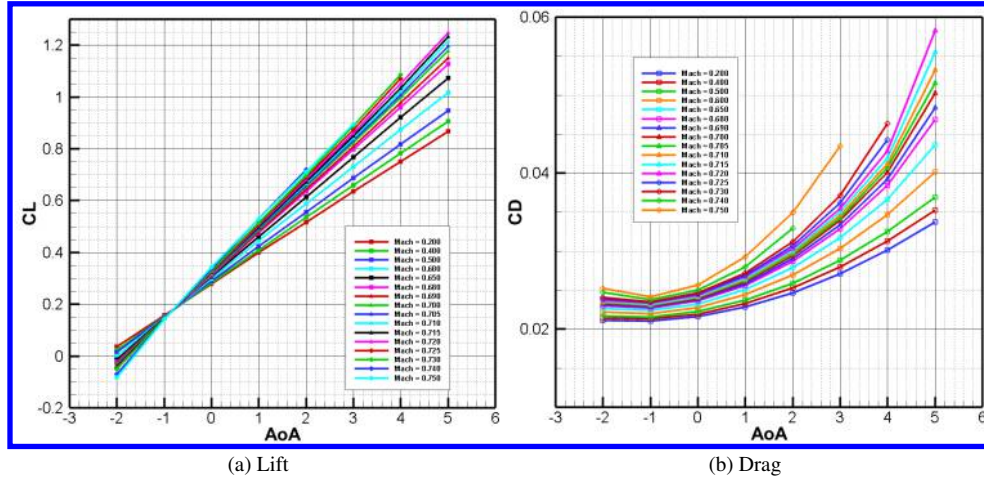


Fig. 20 NSU3D-SA Fully Turbulent Force Coefficient Curves at $Re_{MAC} = 12.3 \times 10^6$ for the S207-Based SNLF TTBW Aircraft

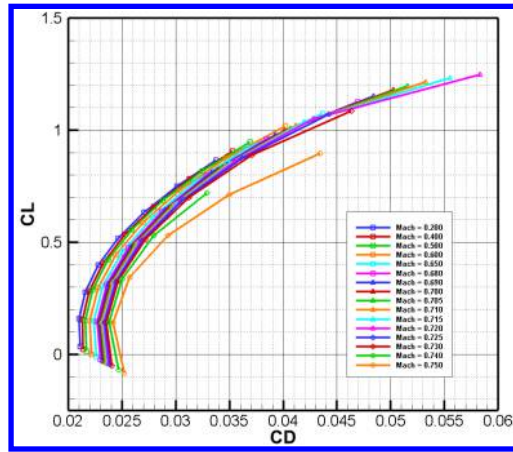


Fig. 21 NSU3D-AFT2-SA Fully Turbulent Drag Polars at $Re_{MAC} = 12.3 \times 10^6$ for the S207-Based SNLF TTBW Aircraft

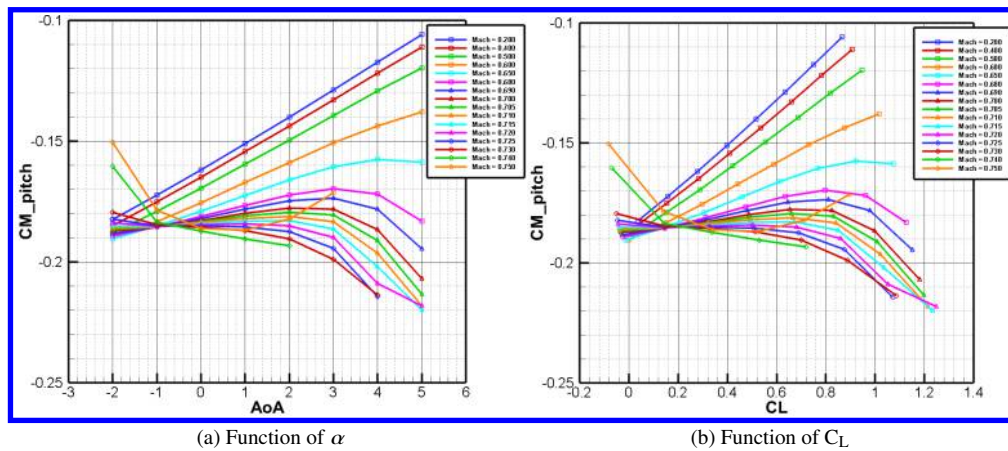


Fig. 22 NSU3D-SA Fully Turbulent Pitching Moment Curves at $Re_{MAC} = 12.3 \times 10^6$ for the S207-Based SNLF TTBW Aircraft

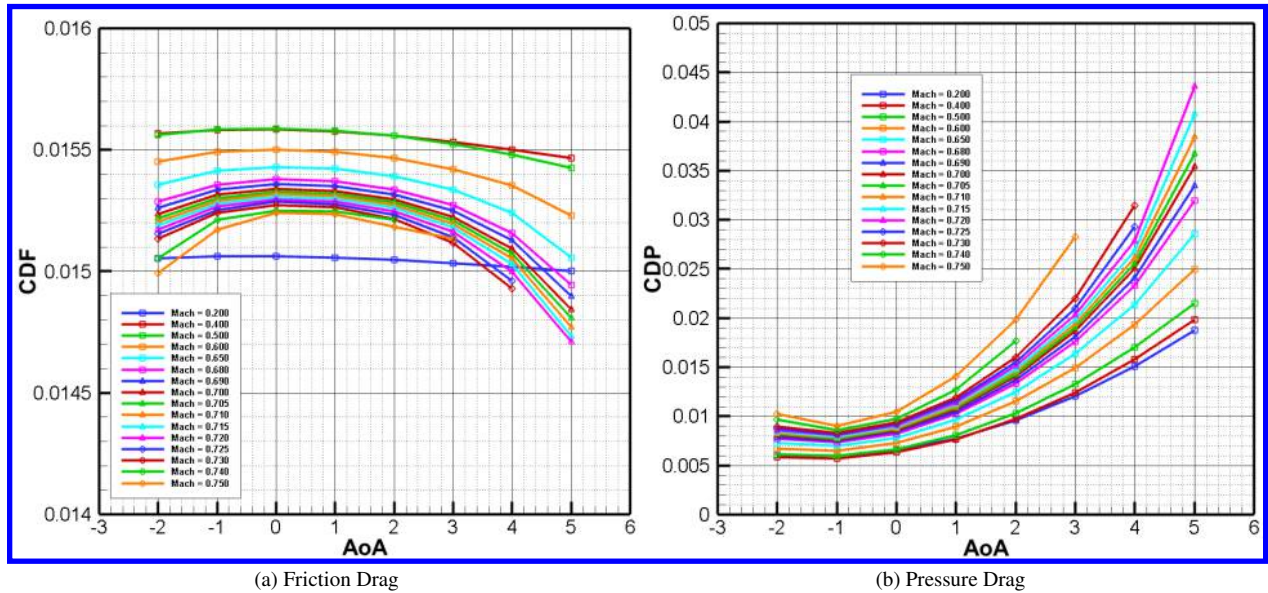


Fig. 23 NSU3D-SA Fully Turbulent Drag Profiles at $Re_{MAC} = 12.3 \times 10^6$ for the S207-Based SNLF TTBW Aircraft

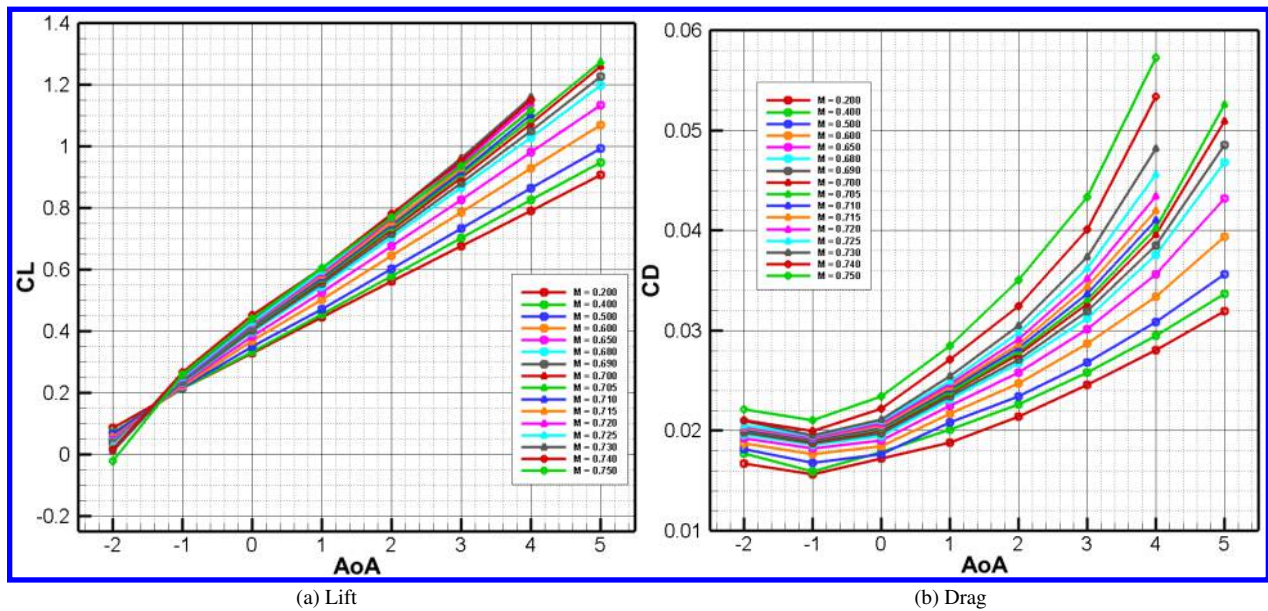


Fig. 24 NSU3D-AFT2-SA Free Transition Force Coefficient Curves with Free Transition Applied to Only the Wing at $Re_{MAC} = 12.3 \times 10^6$ for the S207-Based SNLF TTBW Aircraft

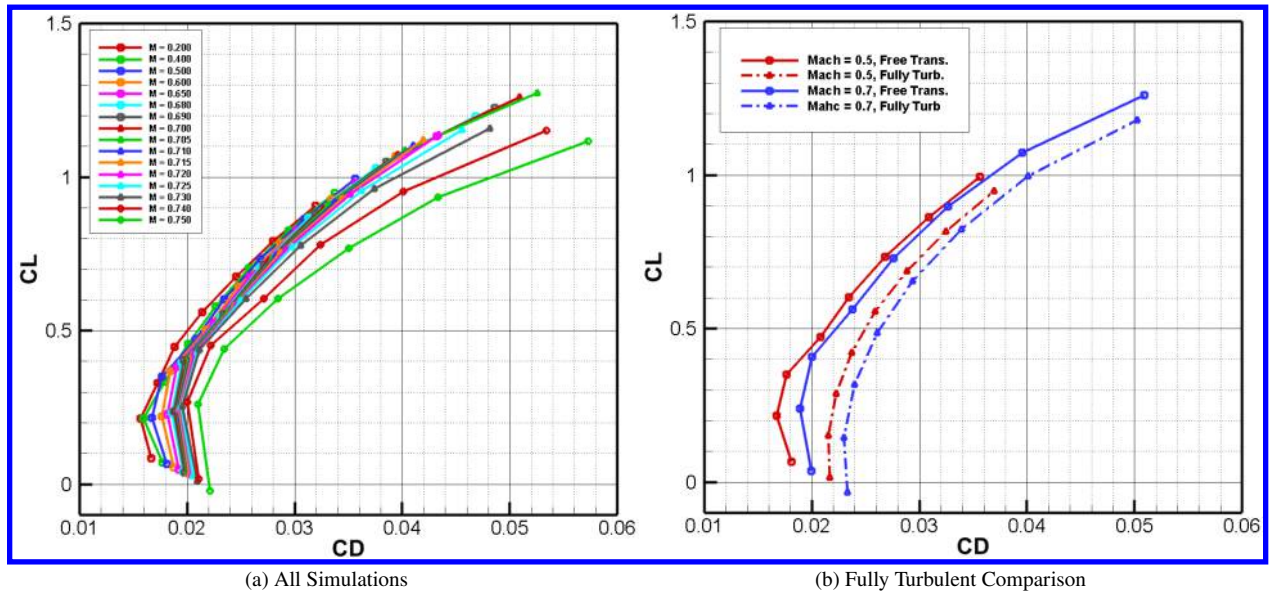


Fig. 25 NSU3D-AFT2-SA Free Transition Drag Polars with Free Transition Applied to Only the Wing at $Re_{MAC} = 12.3 \times 10^6$ for the S207-Based SNLF TTBW Aircraft

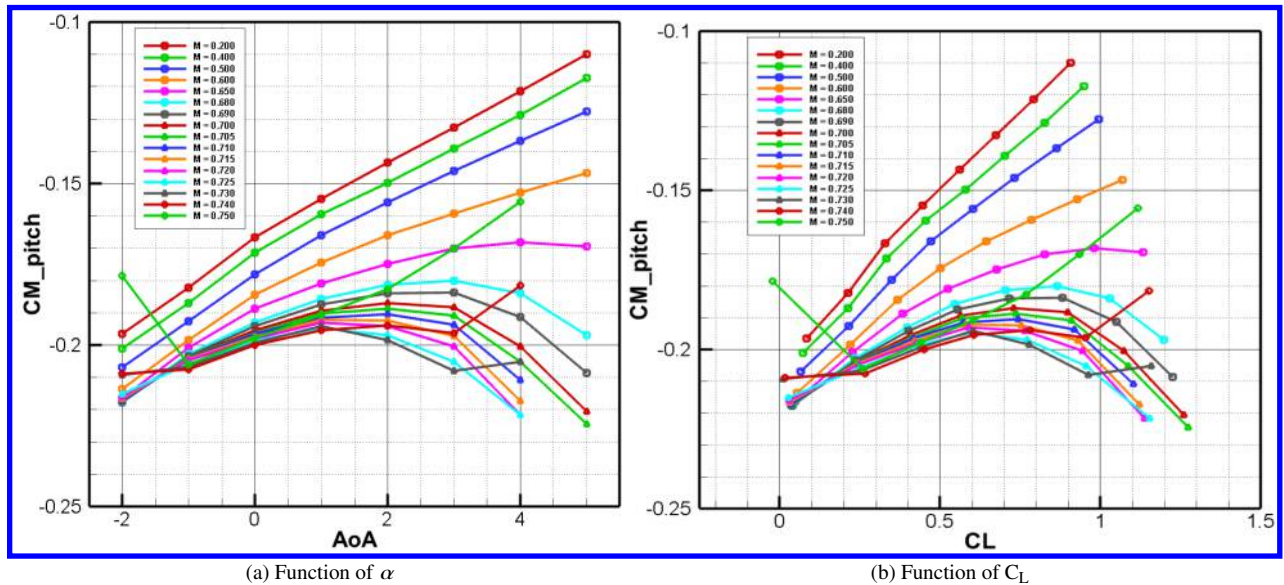


Fig. 26 NSU3D-AFT2-SA Free Transition Pitching Moment Curves with Free Transition Applied to Only the Wing at $Re_{MAC} = 12.3 \times 10^6$ for the S207-Based SNLF TTBW Aircraft

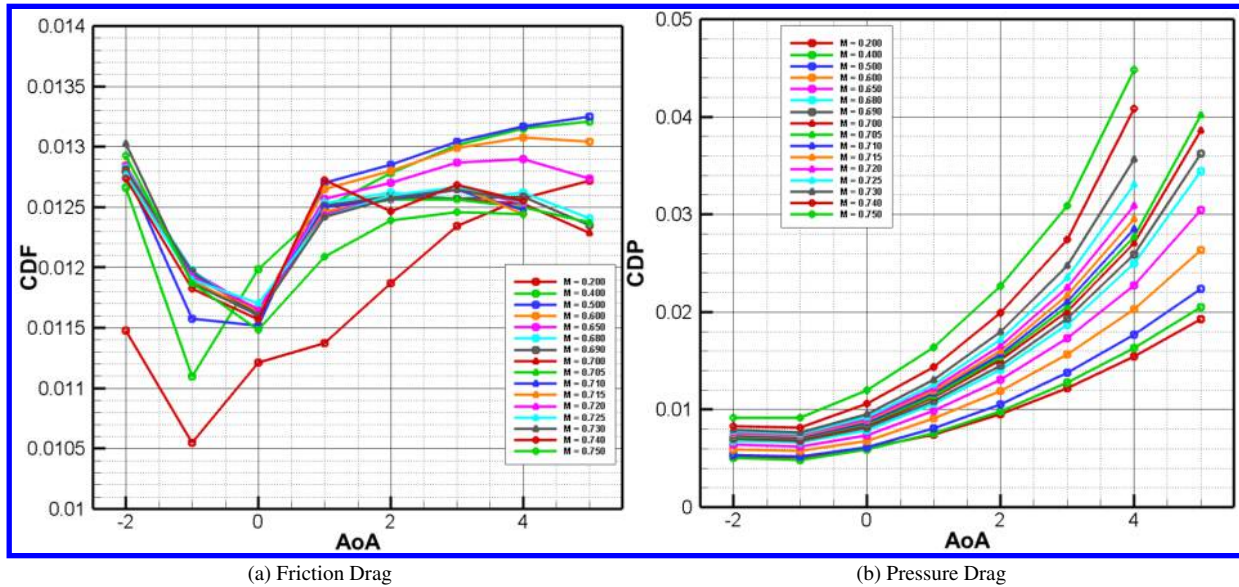


Fig. 27 NSU3D-AFT2-SA Free Transition Drag Profiles with Free Transition Applied to Only the Wing at $Re_{MAC} = 12.3 \times 10^6$ for the S207-Based SNLF TTBW Aircraft

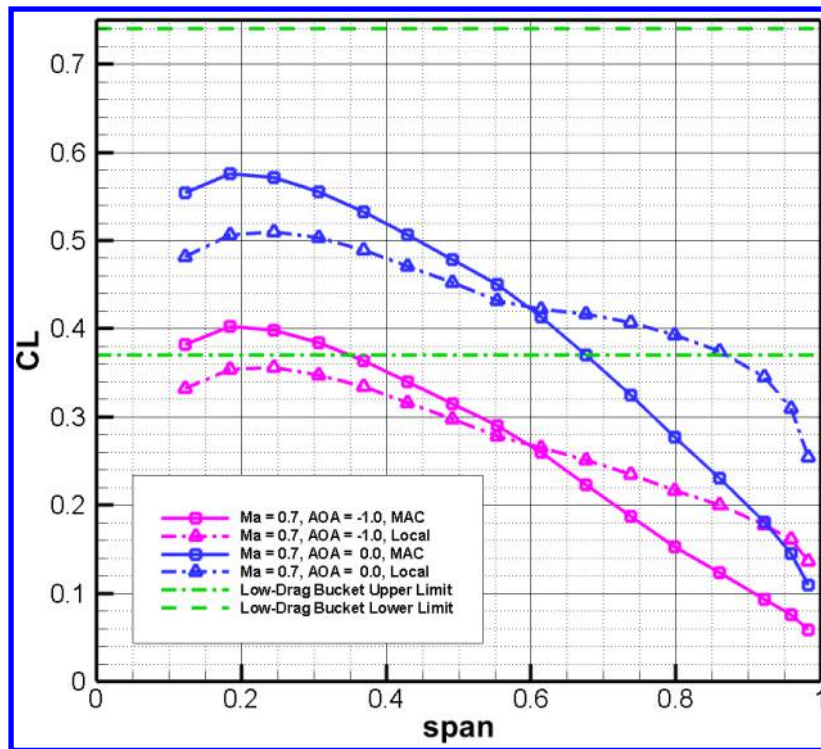


Fig. 28 NSU3D-AFT2-SA Free Transition Spanwise Lift Distributions with Free Transition Applied to Only the Wing at $Re_{MAC} = 12.3 \times 10^6$ for a S207-Based SNLF TTBW Aircraft

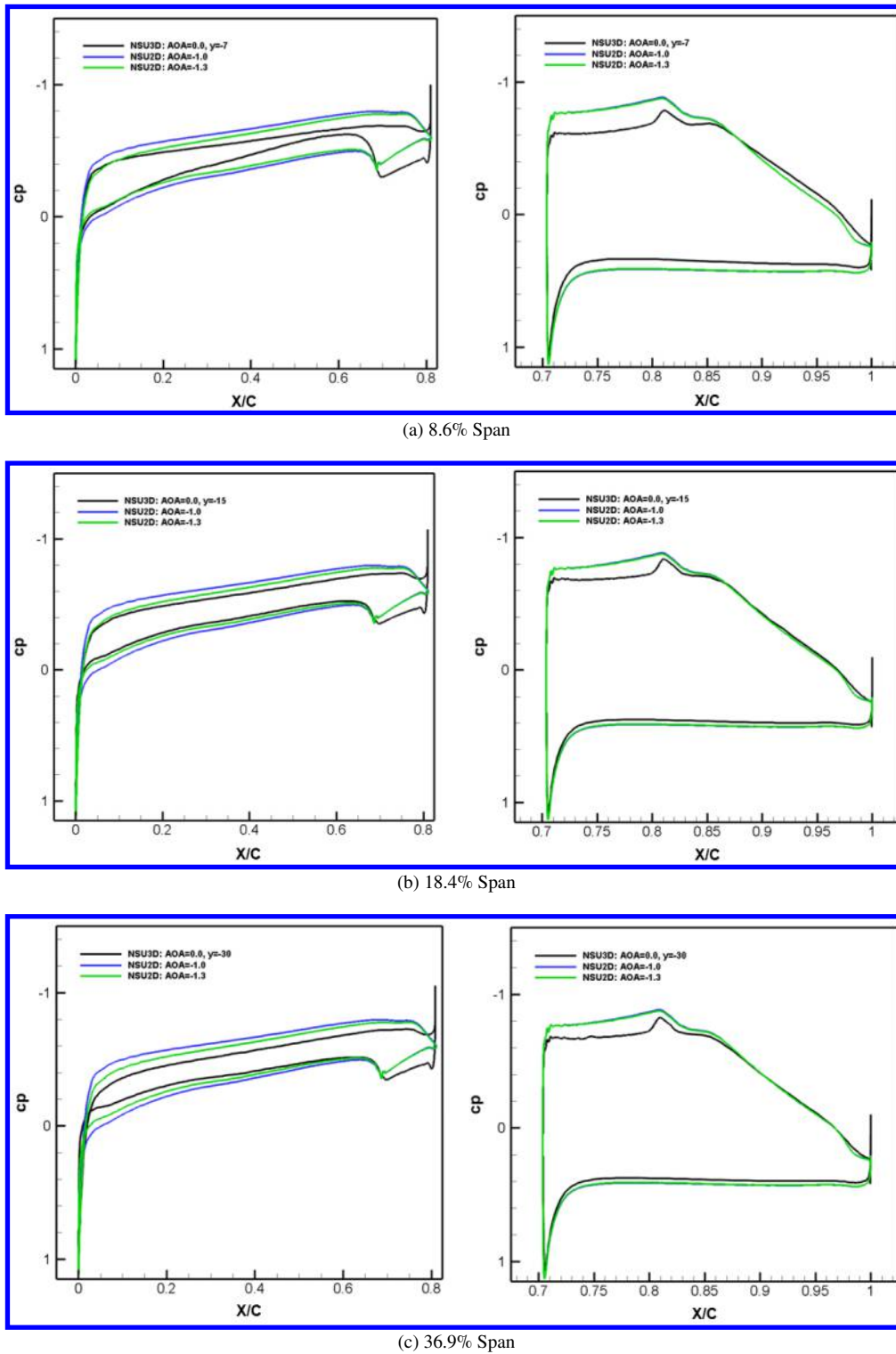


Fig. 29 NSU3D-SA Spanwise Surface Pressure Profiles for a S207-Based TTBW Aircraft at Mach = 0.7, $Re_{MAC} = 12.3 \times 10^6$ Compared to NSU2D-SA Surface Pressure for a 2D S207 Airfoil at Mach = 0.7, $Re_{MAC} = 12.3 \times 10^6$

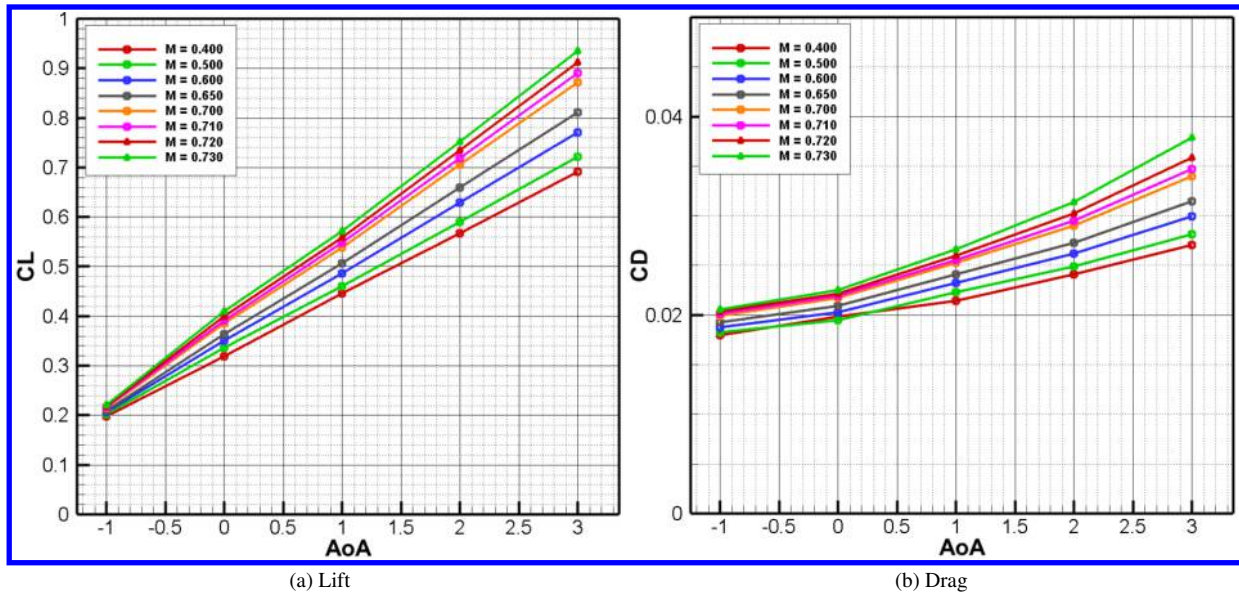


Fig. 30 NSU3D-AFT2-SA Free Transition Force Coefficient Curves with Free Transition Applied Partially to the Wing at $Re_{MAC} = 12.3 \times 10^6$ for the S207-Based SNLF TTBW Aircraft

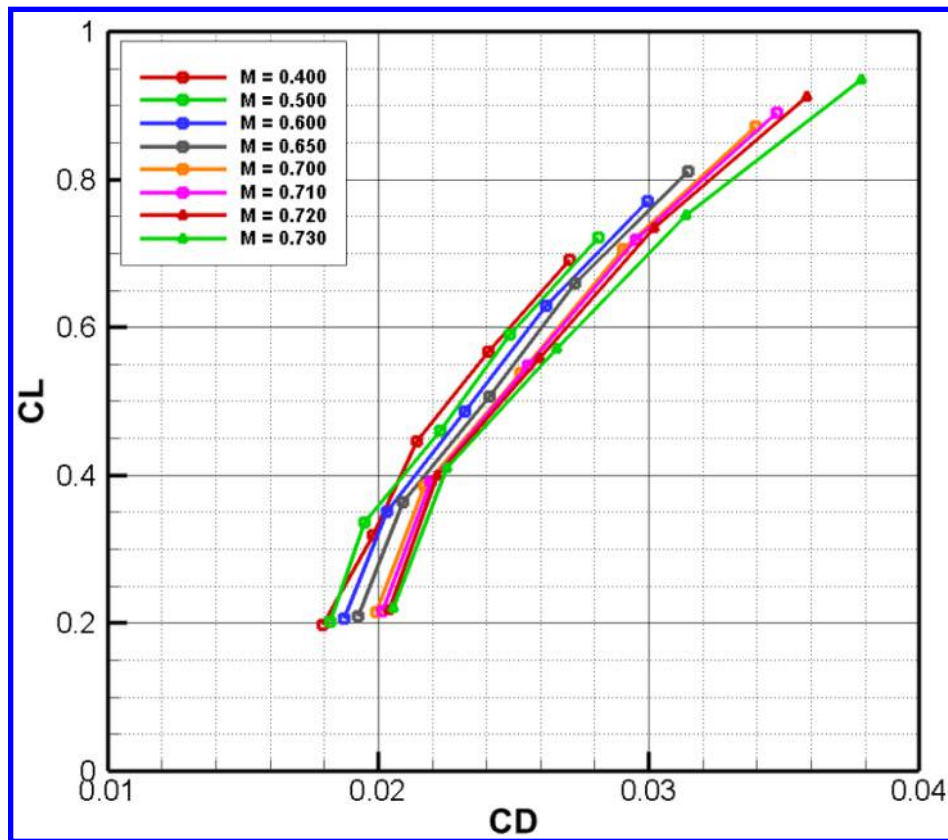


Fig. 31 NSU3D-AFT2-SA Free Transition Drag Polars with Free Transition Applied Partially to the Wing at $Re_{MAC} = 12.3 \times 10^6$ for the S207-Based SNLF TTBW Aircraft

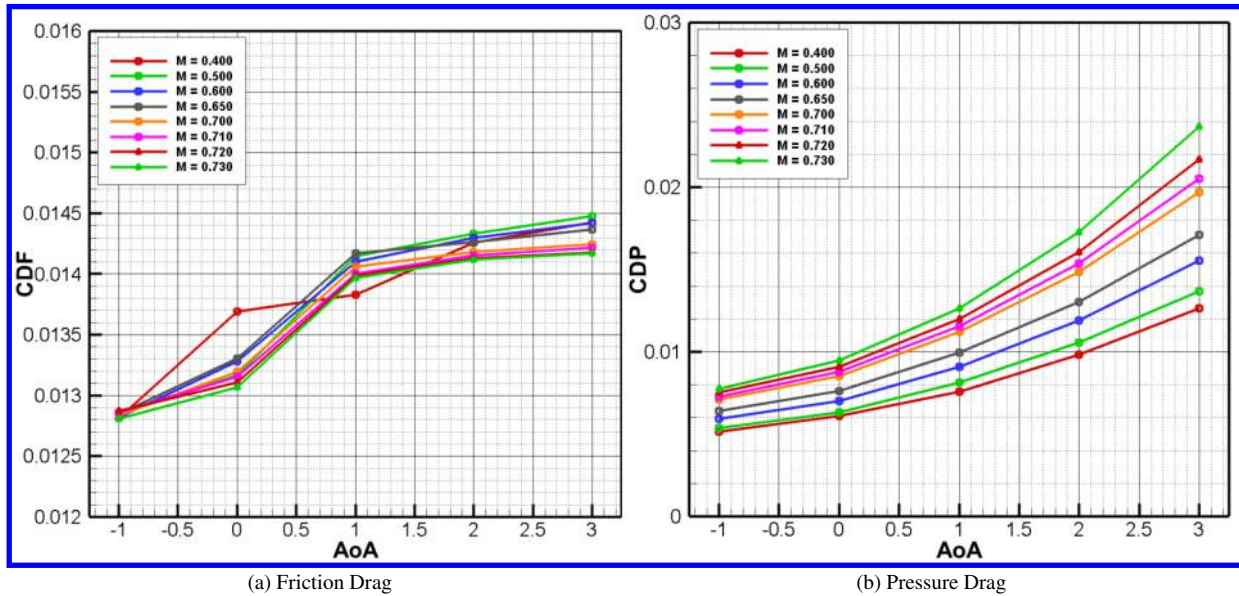


Fig. 32 NSU3D-AFT2-SA Free Transition Drag Profiles with Free Transition Applied Partially to the Wing at $Re_{MAC} = 12.3 \times 10^6$ for the S207-Based SNLF TTBW Aircraft

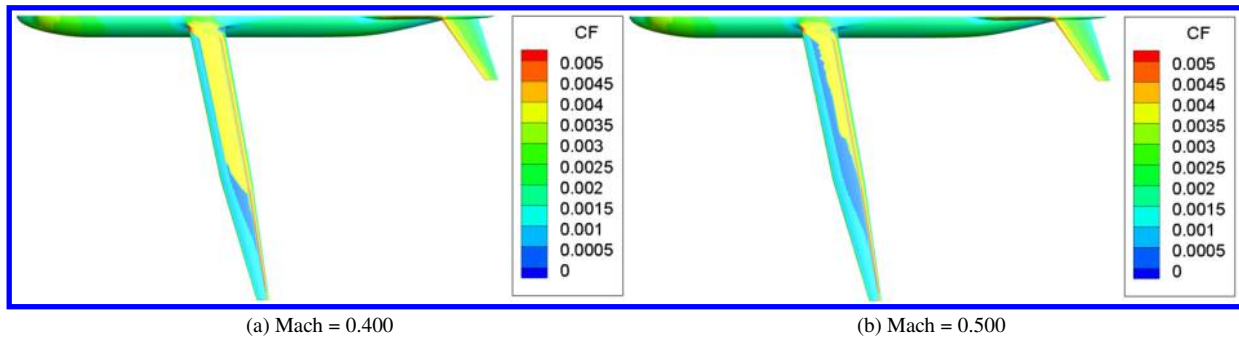


Fig. 33 NSU3D-AAFT2-SA Free Transition C_f Profiles with Free Transition Applied Partially to the Wing at $\alpha = 0^\circ$ and $Re_{MAC} = 12.3 \times 10^6$ for the S207-Based SNLF TTBW Aircraft

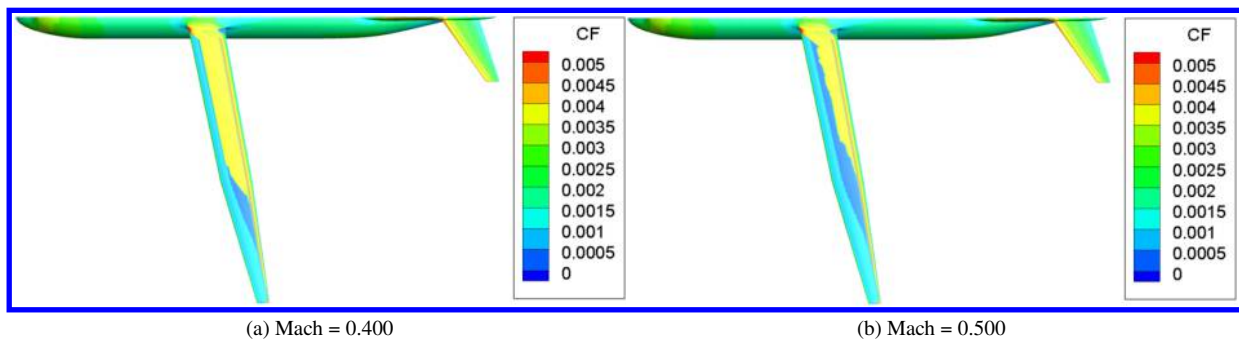


Fig. 34 NSU3D-AFT2-SA Free Transition C_f Profiles with Free Transition Applied to Only the Wing at $\alpha = 0^\circ$ and $Re_{MAC} = 12.3 \times 10^6$ for the S207-Based SNLF TTBW Aircraft

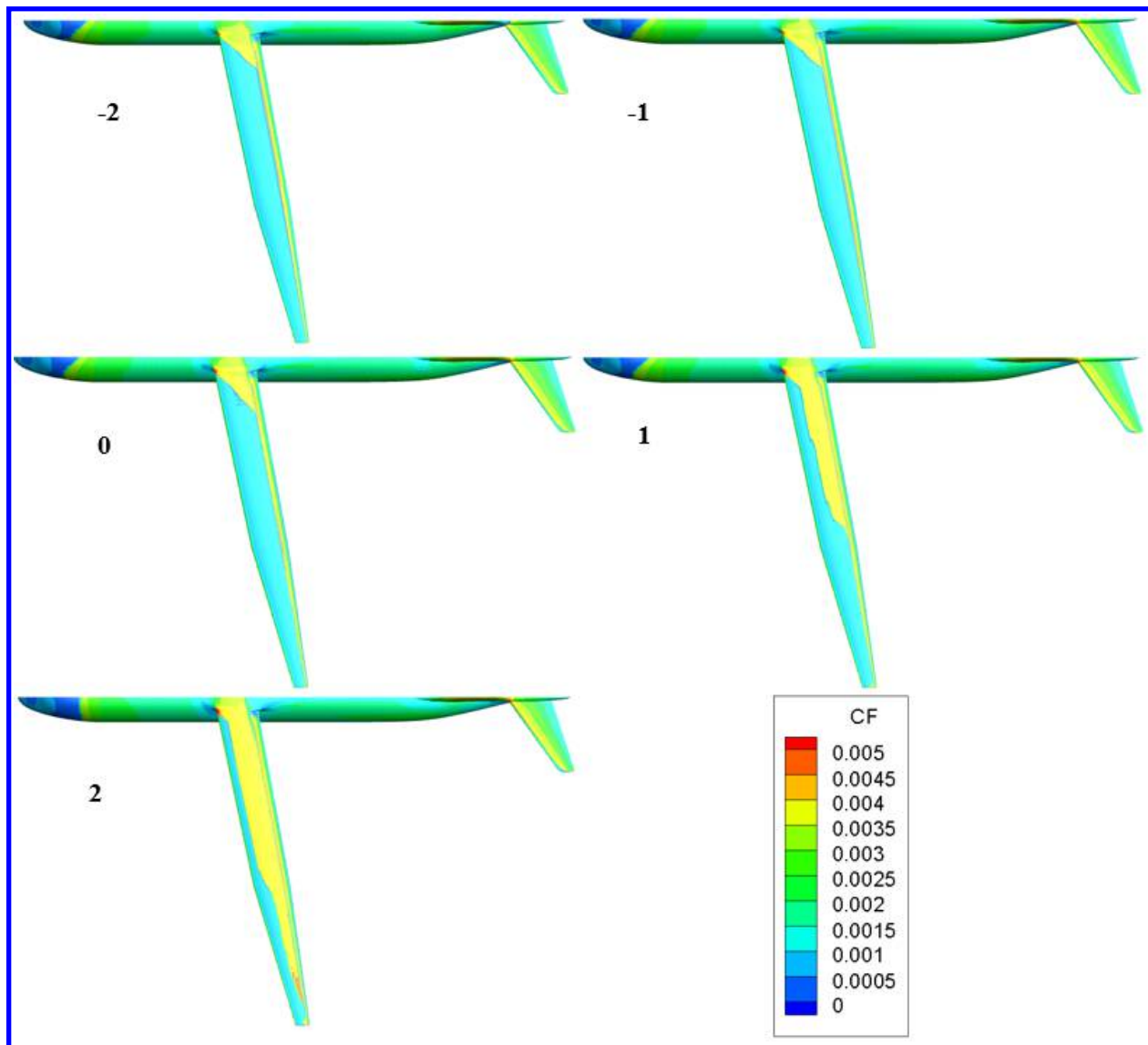


Fig. 35 NSU3D-AFT2-SA Free Transition Upper Surface C_f Contours at Mach = 0.7273, $Re_{MAC} = 12.3 \times 10^6$, and $N_{crit} = 10.4$ ($Tu_\infty = 0.039\%$) for the S207-Based SNLF TTBW Aircraft

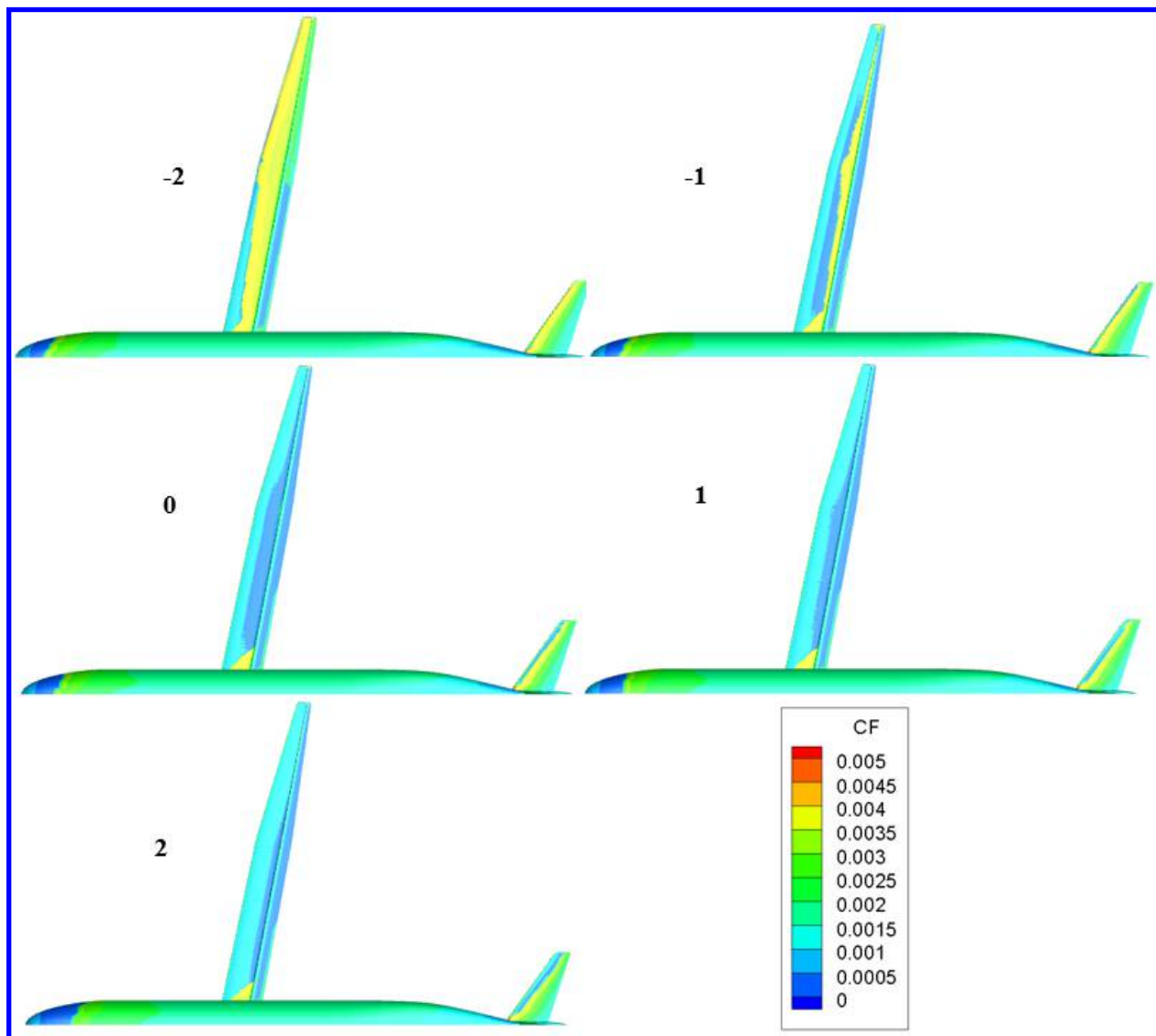


Fig. 36 NSU3D-AFT2-SA Free Transition Lower Surface C_f Contours at Mach = 0.7273, $Re_{MAC} = 12.3 \times 10^6$, and $N_{crit} = 10.4$ ($Tu_\infty = 0.039\%$) for the S207-Based SNLF TTBW Aircraft

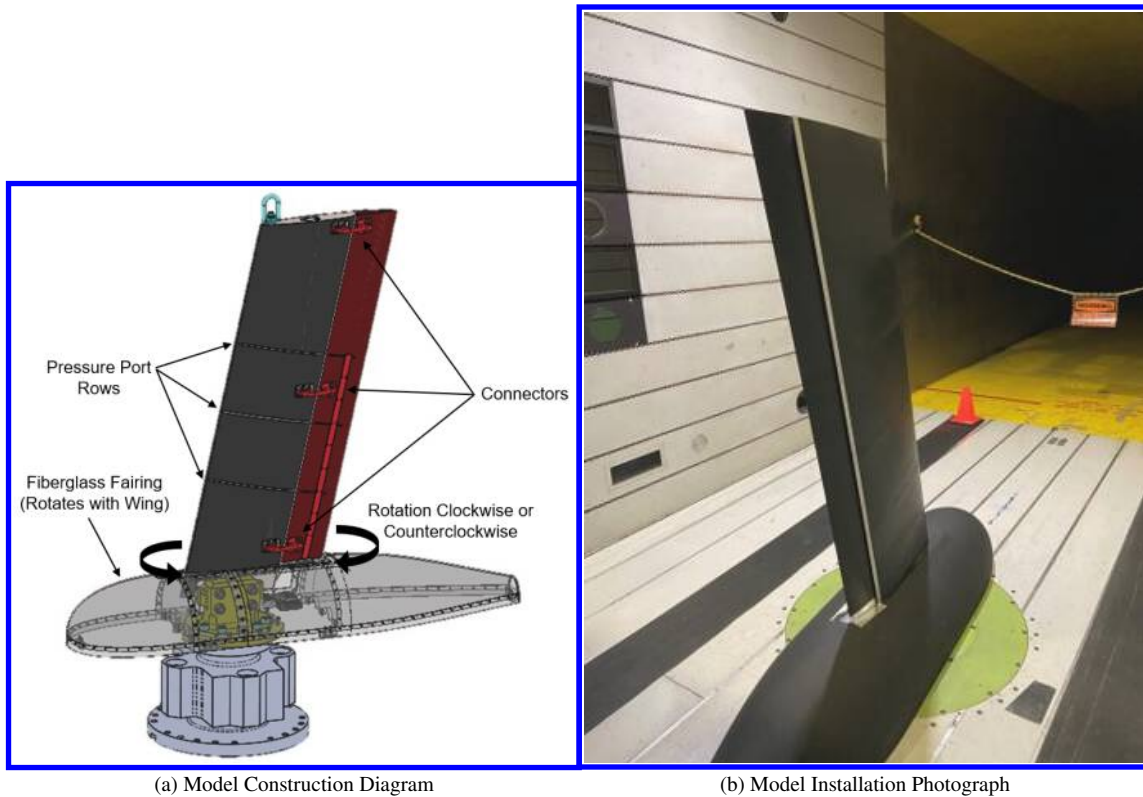


Fig. 37 Wind Tunnel Model Details

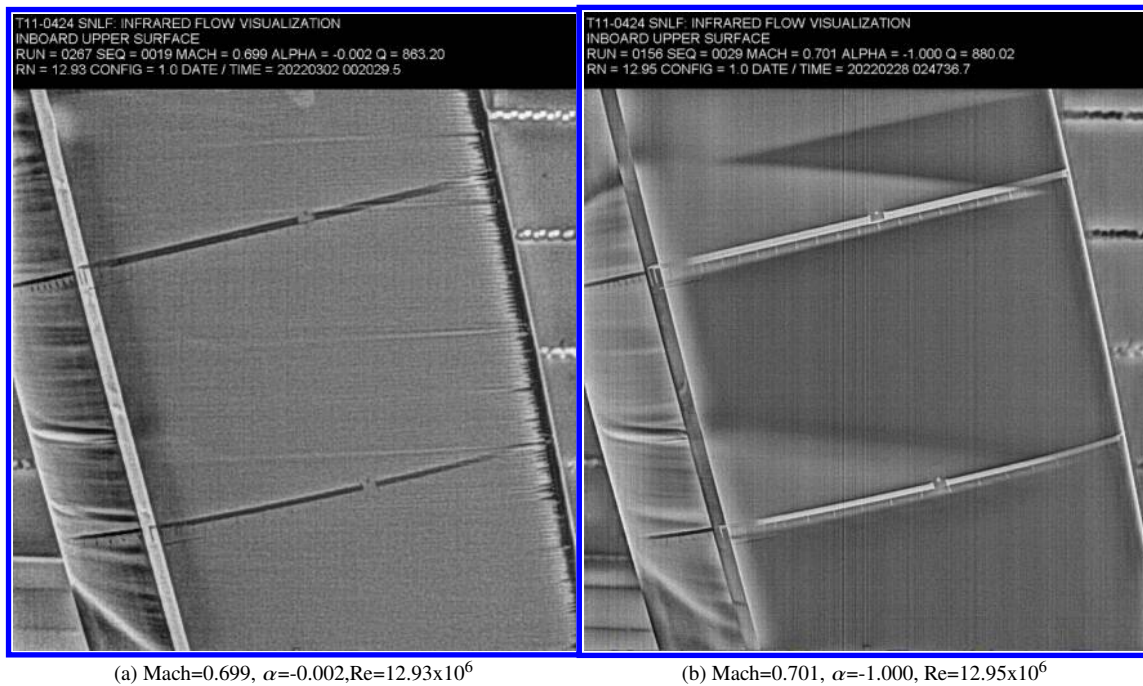
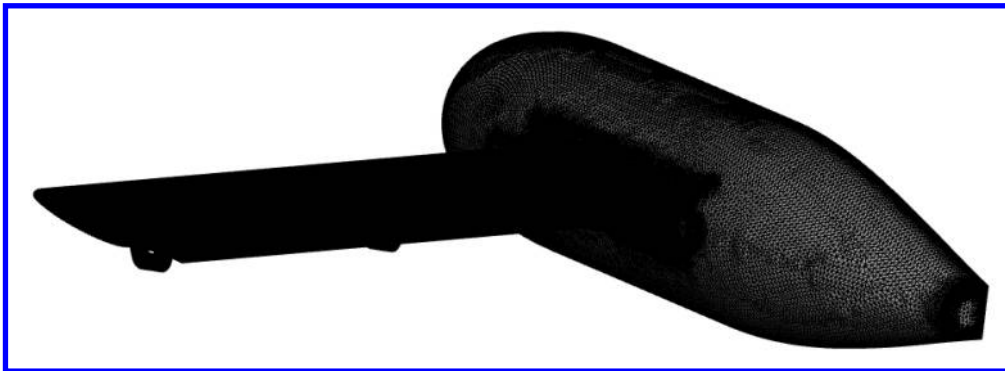
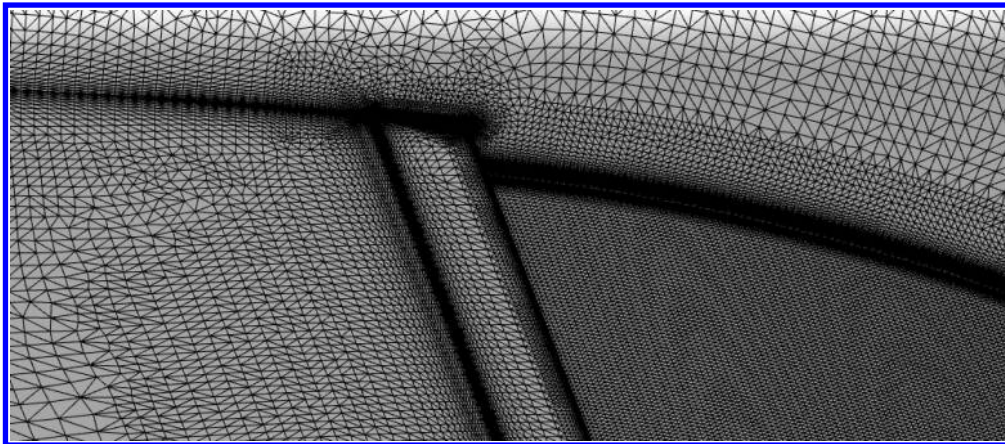


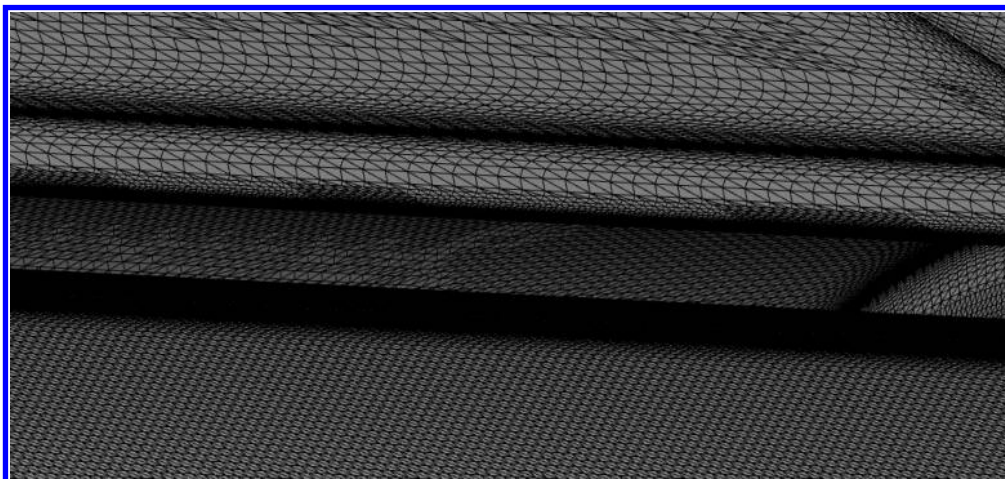
Fig. 38 IR Images of Right to Left Moving Flow on the Upper Surface of the Wing Near the Fairing with Evident Transition Lines for $\alpha = -1.000^\circ$



(a) Wing-Fairing Model

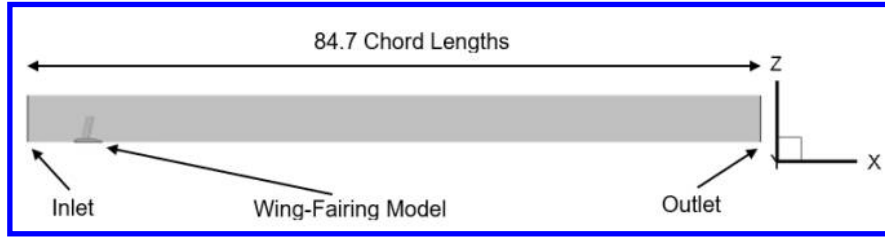


(b) Wing-Fairing Junction

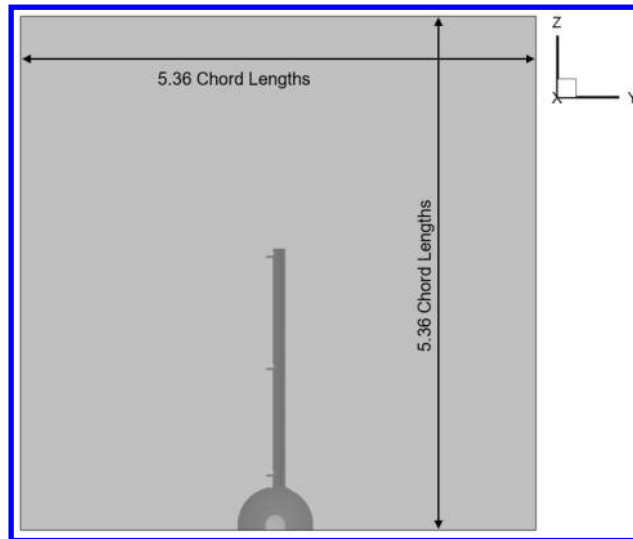


(c) Slot at Wing-Fairing Junction

Fig. 39 Wind Tunnel Model Computational Mesh



(a) Full Channel



(b) Channel Inlet View

Fig. 40 Wind Tunnel Channel Specifications

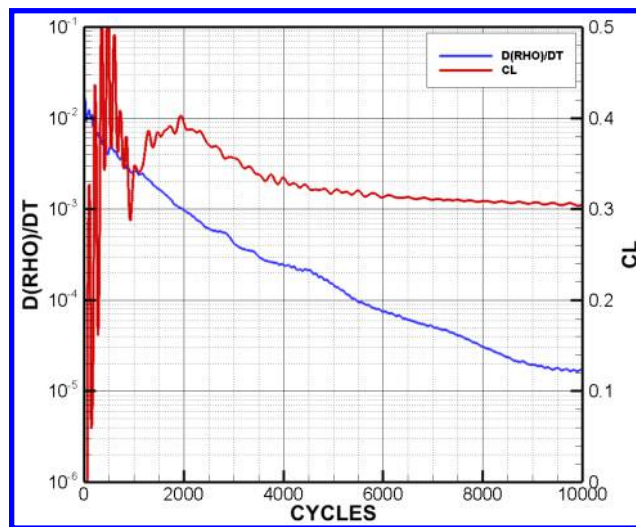


Fig. 41 NSU3D-SA Fully Turbulent Wind Tunnel Model Solution Convergence History at Mach=0.7, $\alpha=0^\circ$, $Re=12 \times 10^6$

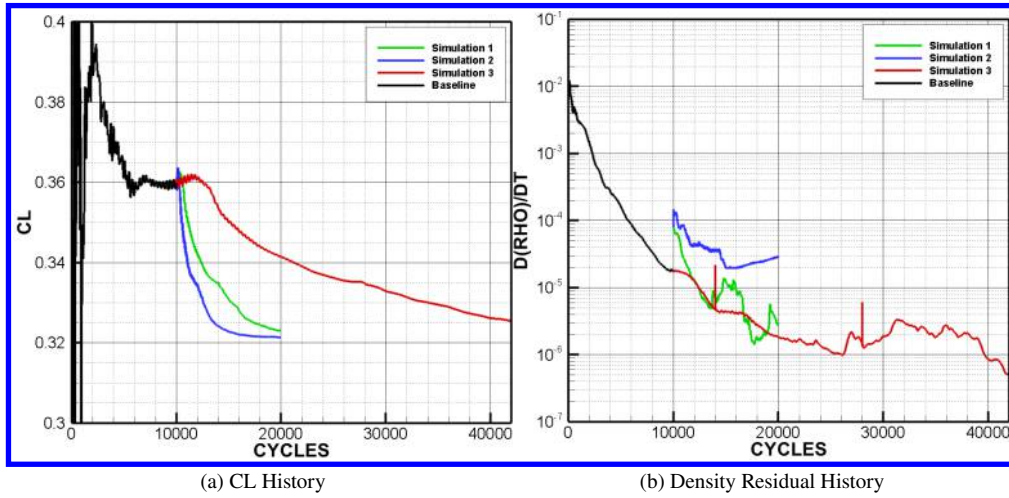


Fig. 42 NSU3D-AFT2-SA Free Transition Wind Tunnel Model Simulation Histories at Mach = 0.7, $\alpha = 0^\circ$, $Re = 12 \times 10^6$, and $N_{crit} = 8.4$ ($Tu_\infty = 0.09\%$)

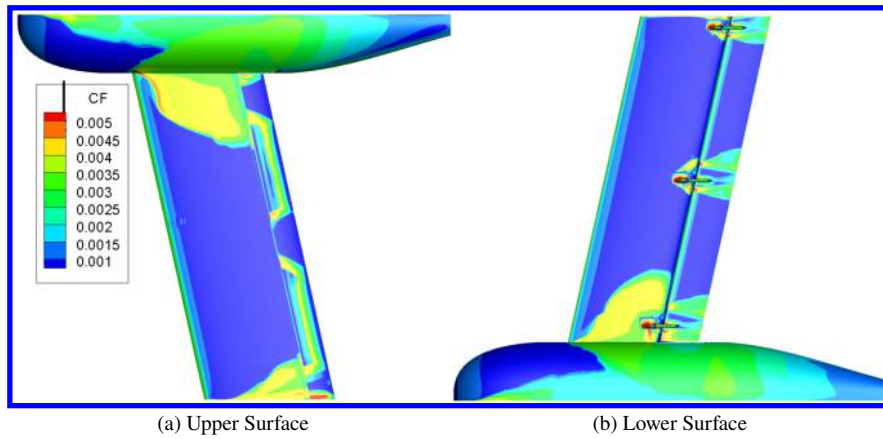


Fig. 43 NSU3D-AFT2-SA C_f Distribution for Baseline solution at Mach = 0.7, $\alpha = 0^\circ$, $Re = 12 \times 10^6$, and $N_{crit} = 8.4$ ($Tu_\infty = 0.09\%$)

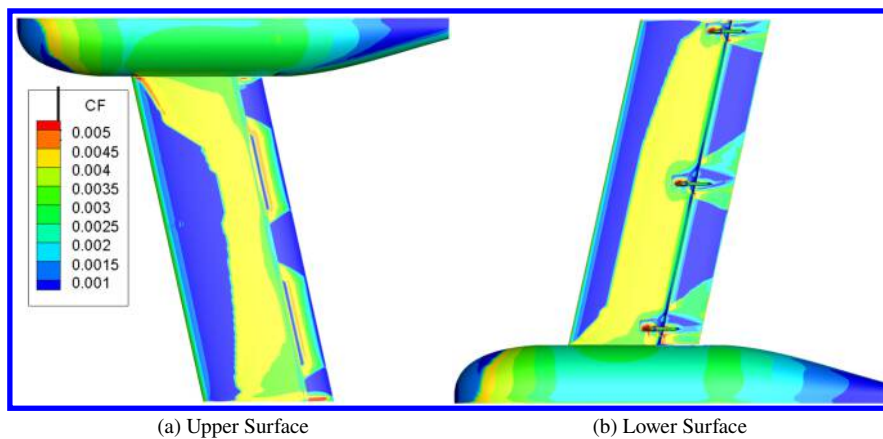


Fig. 44 NSU3D-AFT2-SA C_f Distribution for Simulation 1 at Mach = 0.7, $\alpha = 0^\circ$, $Re = 12 \times 10^6$, and $N_{crit} = 8.4$ ($Tu_\infty = 0.09\%$)

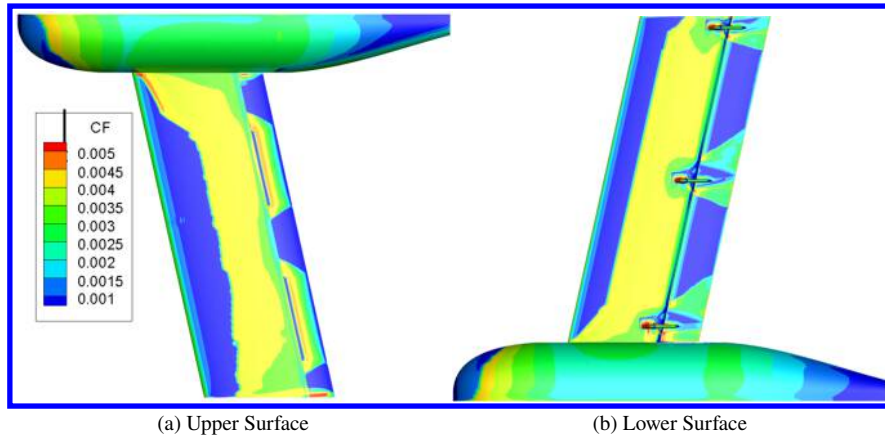


Fig. 45 NSU3D-AFT2-SA C_f Distribution for Simulation 2 at Mach = 0.7, $\alpha = 0^\circ$, $Re = 12 \times 10^6$, and $N_{crit} = 8.4$ ($Tu_\infty = 0.09\%$)

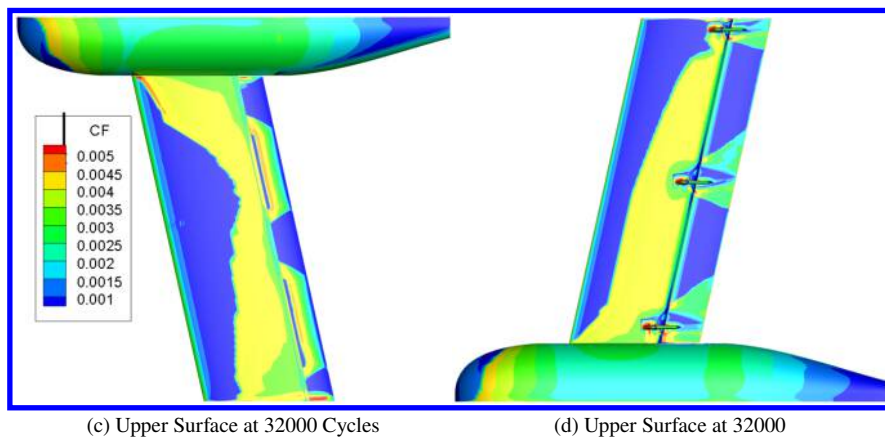
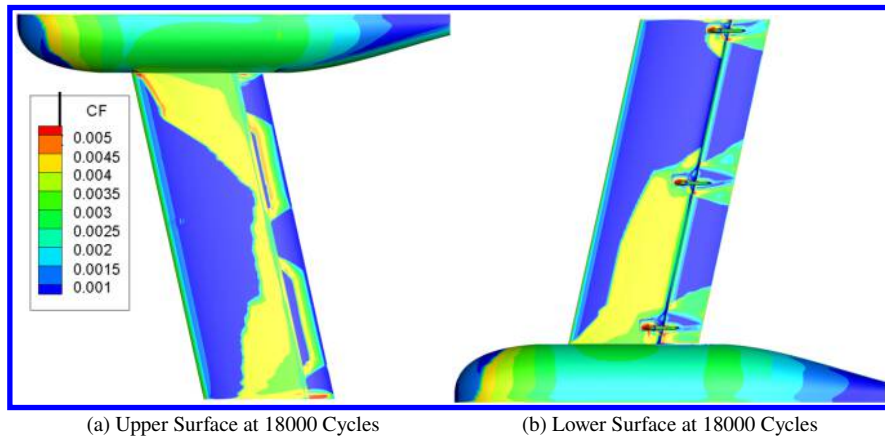


Fig. 46 NSU3D-AFT2-SA C_f Distributions for Simulation 3 at Mach = 0.7, $\alpha = 0^\circ$, $Re = 12 \times 10^6$, and $N_{crit} = 8.4$ ($Tu_\infty = 0.09\%$)

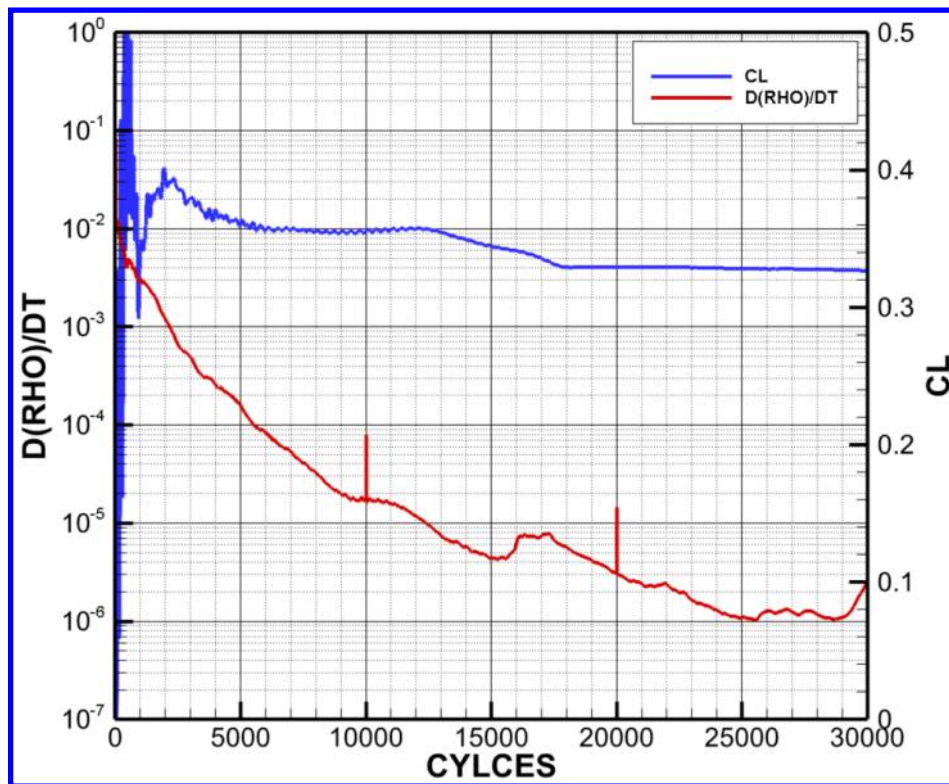


Fig. 47 NSU3D-AFT2-SA Free Transition Wind Tunnel Model Solution Convergence History at Mach = 0.7, $\alpha = 0^\circ$, $Re = 12 \times 10^6$, and $N_{crit} = 6$ ($Tu_\infty = 0.245\%$)

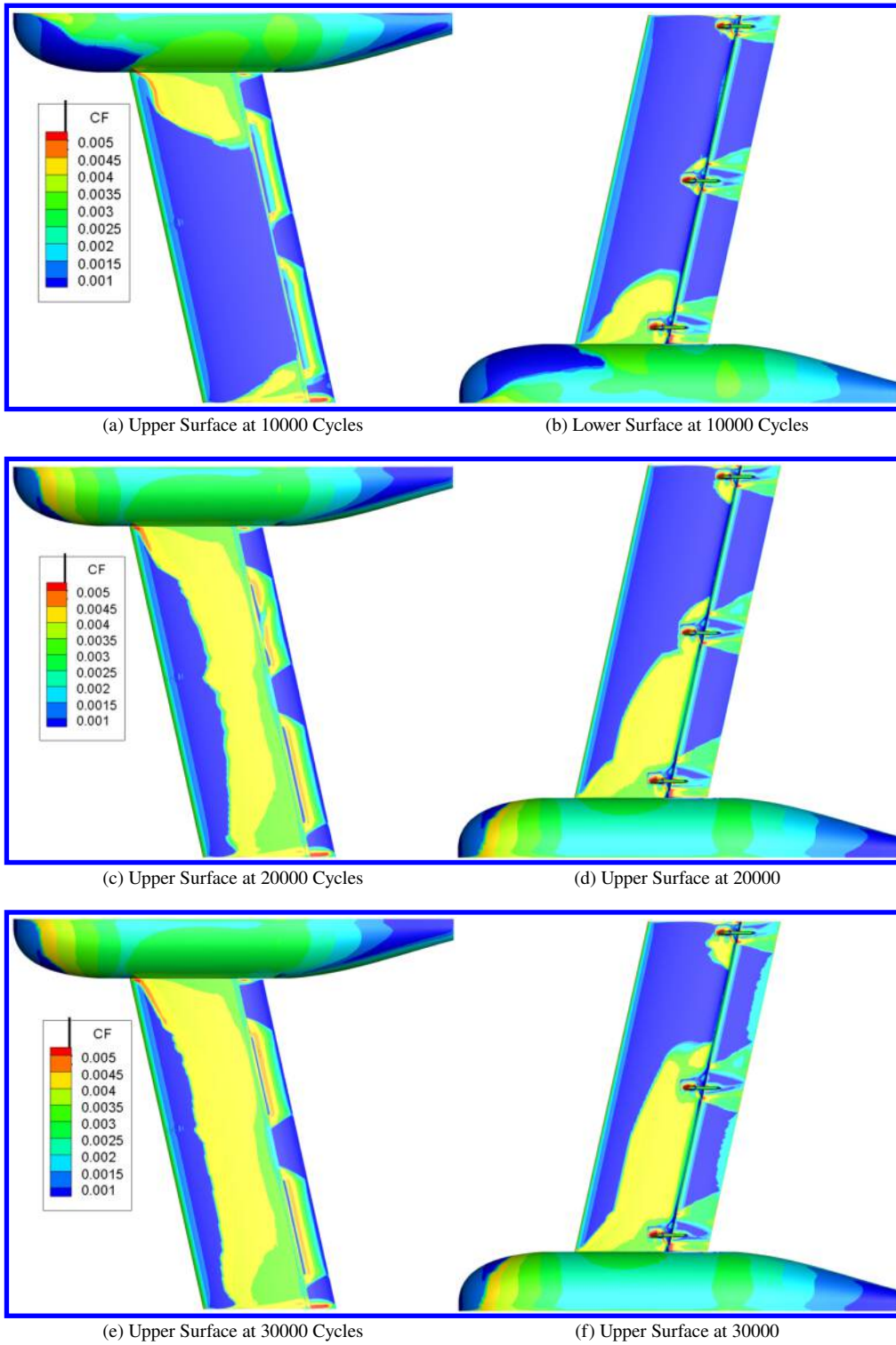


Fig. 48 NSU3D-AFT2-SA C_f Distributions at Mach = 0.7, $\alpha = 0^\circ$, $Re = 12 \times 10^6$, and $N_{crit} = 6.0$ ($Tu_\infty = 0.245\%$)

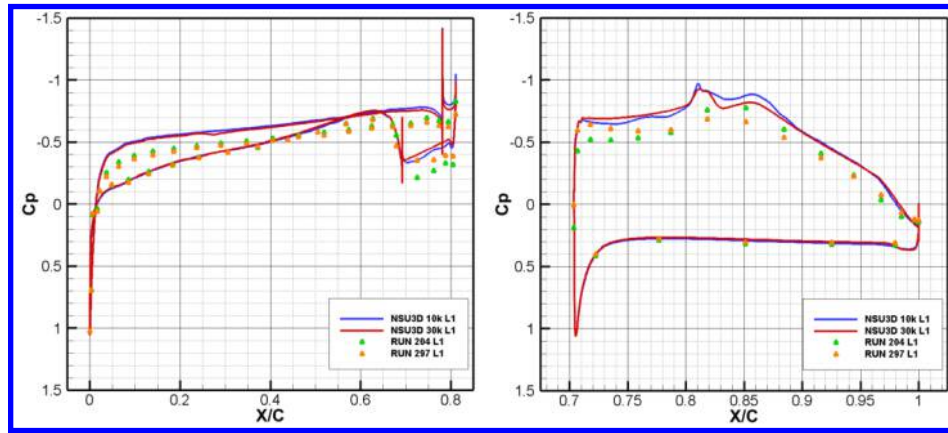
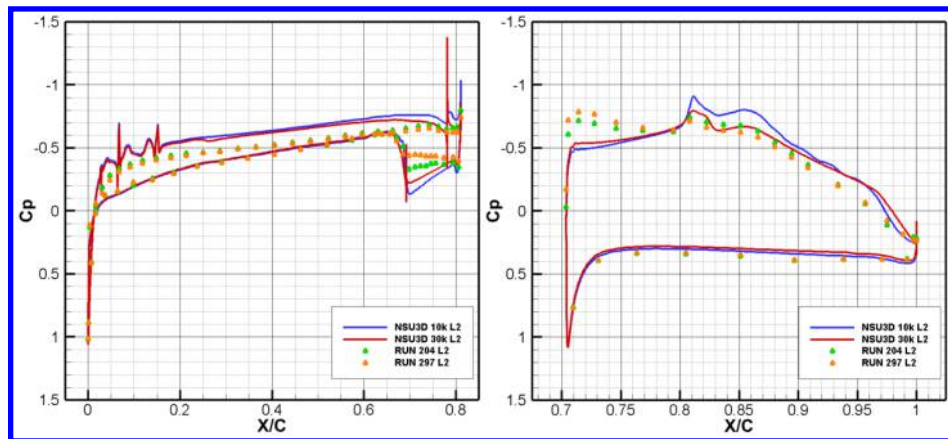
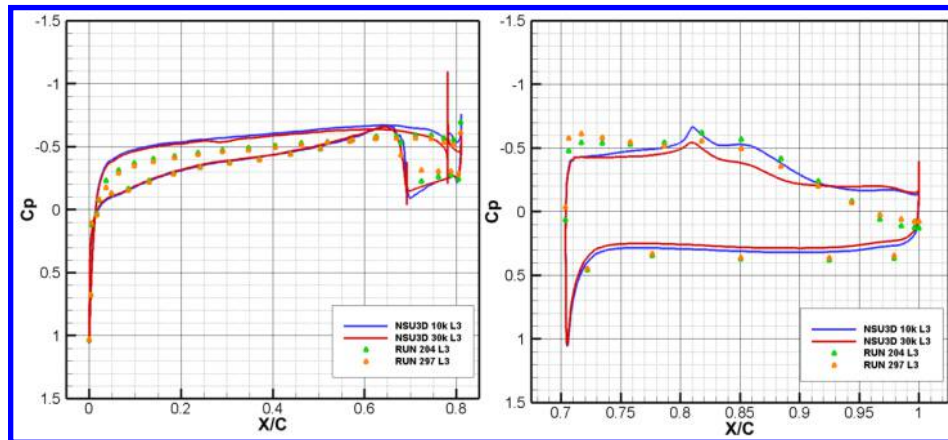
(a) Surface C_p Distributions at Inboard Pressure Port Location L1(b) Surface C_p Distributions at Midboard Pressure Port Location L2(c) Surface C_p Distributions at Outboard Pressure Port Location L3

Fig. 49 NSU3D-AFT2-SA $N_{crit} = 6.0$ ($Tu_{\infty} = 0.245\%$) vs. Ames Wind Tunnel Data Surface Pressure Distributions at $Mach = 0.7$, $\alpha = 0^\circ$

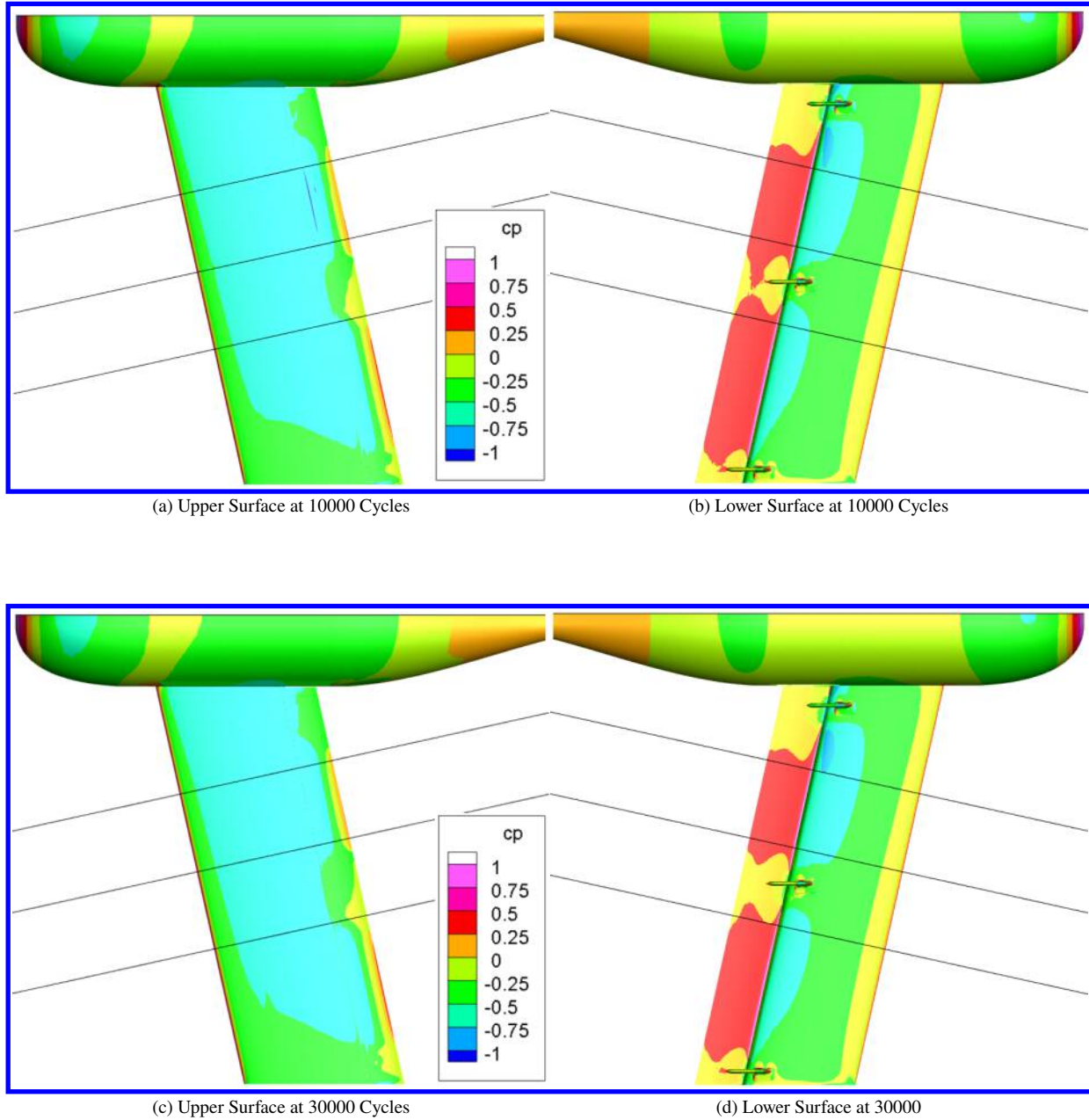


Fig. 50 NSU3D-AFT2-SA Surface Pressure Distributions for Mach = 0.7, $\alpha = 0^\circ$, $Re = 12 \times 10^6$, and $N_{crit} = 6$ ($Tu_\infty = 0.245\%$)

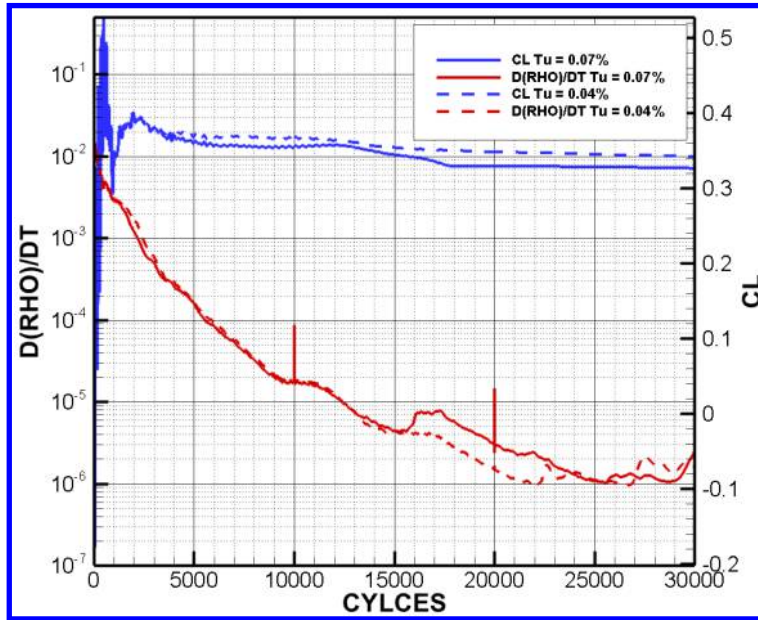


Fig. 51 Wind Tunnel Model Simulation Convergence Comparison for Varying Freestream Turbulence Intensity

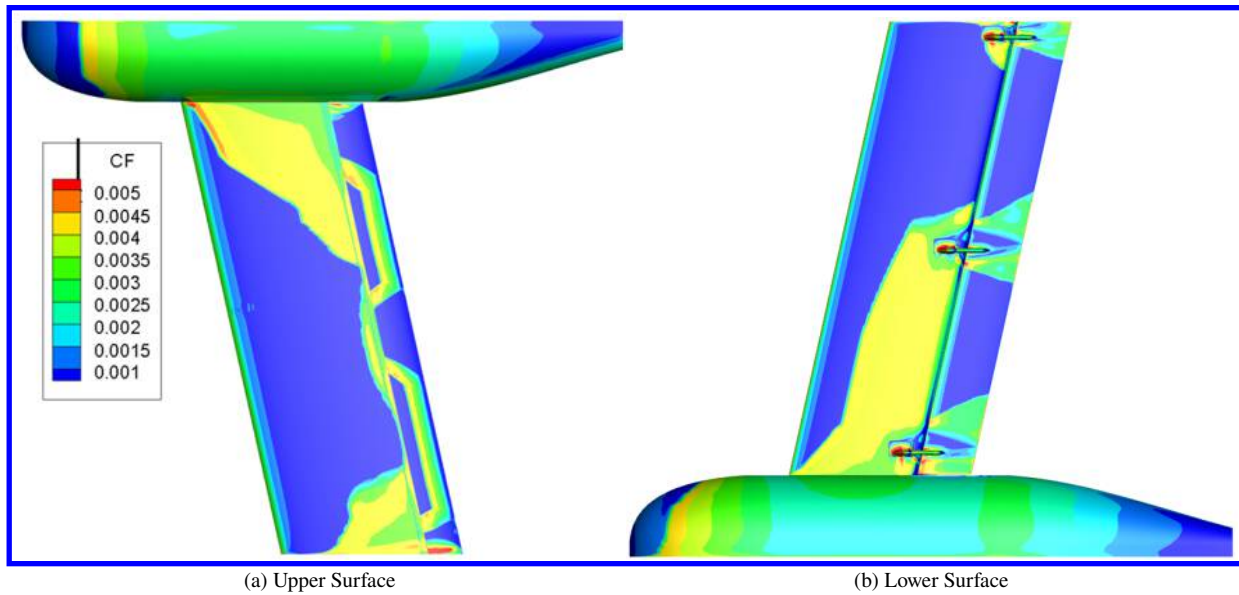


Fig. 52 NSU3D-AFT2-SA C_f Distribution at Mach = 0.7, $\alpha = 0$, $Re = 12 \times 10^6$, and $N_{crit} = 10.4$ ($Tu_\infty = 0.039\%$)

VII. Acknowledgments

This work was supported by the National Aeronautics and Space Administration (NASA) University Leadership Initiative (ULI) "Advanced Aerodynamics Design Center for Ultra-Efficient Commercial Vehicles" (Award NNX17AJ95A) led by the University of Tennessee at Knoxville. Thanks are extended to the NASA ULI Vision-Vehicle Integration Subgroup. This work would not have been possible without their consistent collaboration efforts. Additional thanks is given to both the University of Wyoming ARCC and the NCAR Wyoming Supercomputer Alliance for computer time.

References

- [1] International Energy Agency, “CO₂ Emissions From Fuel Combustion: Highlights,” 2019, Accessed Nov., 2022. URL: https://iea.blob.core.windows.net/assets/eb3b2e8d-28e0-47fd-a8ba-160f7ed42bc3/CO2_Emissions_from_Fuel_Combustion_2019_Highlights.pdf.
- [2] S. Gossling and A. Humpe, “The Global Scale, Distribution and Growth of Aviation: Implications for Climate Change,” *Global Environmental Change*, Vol. 65, 2021, doi: <https://doi.org/10.1016/j.gloenvcha.2020.102194>.
- [3] NASA Aeronautics, “Strategic Implementation Plan: 2019 Update,” 2019, Accessed Aug., 2021. URL: <https://nasa.gov/aeroresearch/strategy>.
- [4] S. Gudmundsson, “Aircraft Drag Analysis,” *General Aviation Aircraft Design*, Butterworth-Heinemann, 2014, pp. 661–760, doi: <http://dx.doi.org/10.1016/B978-0-12-397308-5.00015-5>.
- [5] D. Somers, “Laminar Flow Airfoil,” US Patent 6905092 B2, June 14, 2005.
- [6] Somers, D., “An Exploratory Investigation of a Slotted, Natural-Laminar-Flow Airfoil,” NASA/CR-2012-217560, July, 2012.
- [7] Somers, D., “Design of a Slotted, Natural-Laminar-Flow Airfoil for Business Jet Applications,” NASA/CR-20120217559, April, 2012.
- [8] D. Somers, “Design of a Slotted, Natural-Laminar-Flow Airfoil for Transport Aircraft,” NASA/CR-2019-220403, June, 2019.
- [9] J. Coder and D. Somers, “Design of a Slotted, Natural-Laminar-Flow Airfoil for Commercial Transport Applications,” *Aerospace Science and Technology*, Vol. 106, Nov. 2020, doi: <https://doi.org/10.1016/j.ast.2020.106217>.
- [10] J. Coder, M. Maughmer and D. Somers, “Theoretical and Experimental Results for the S414, Slotted, Natural-Laminar-Flow Airfoil,” *Journal of Aircraft*, Vol. 51, No. 6, Nov. 2014, pp. 1883–1890, doi: <https://doi.org/10.2514/1.C032566>.
- [11] M. Maughmer, J. Coder and D. Somers, “Exploration of a Slotted, Natural-Laminar-Flow Airfoil Concept,” AIAA Paper 2018-3815, 2018 Applied Aerodynamics Conference, July 25–29, Atlanta, GA. doi: <https://doi.org/10.2514/6.2018-3815>.
- [12] M. Drela, “A User’s Guide to MSES 3.05,” MIT Department of Aeronautics and Astronautics, July 2007.
- [13] M. Bradley and C. Droney, “Subsonic Ultra Green Aircraft Research Phase 2: N+4 Advanced Concept Development,” NASA/CR-20120217556, May, 2012.
- [14] J. Coder, “Advanced Aerodynamic Design Center for ultra-Efficient Commercial Vehicles: ARMD Strategic Thrust: Ultra-Efficient Commercial Vehicles (Thrust 3A),” Presented at the University Leadership Initiative Annual Review, Sep., 2021.
- [15] P. Camacho, K. Pham, L. Chou, N Harrison and A. Khodadoust, “Progress on Aerodynamic Performance Analysis of SNLF Transonic Truss-Braced Wing,” AIAA Paper 2020-1025, 2020 AIAA SciTech Forum, Jan. 6–10, Orlando, FL. doi: <https://doi.org/10.2514/6.2020-1025>.
- [16] C. Perkins, Z. Yang, I. Topcuoglu, D. Mavriplis, J. Coder, E. Hereth, and C. Axten, “Aerodynamic Analysis of a Slotted, Natural-Laminar-Flow Transonic Trussed-Braced Wing Aircraft Configuration,” AIAA Paper 2022-2536, 2021 AIAA SciTech Forum, Jan 3rd–7th, San Diego, CA. doi: <https://doi.org/10.2514/6.2022-2536>.
- [17] F. Menter, P. Smirnov, and T. Liu, “A One-Equation Local Correlation-Based Transition,” *Flow, Turbulence and Combustion*, Vol. 95, No. 1, 2015, pp. 593–619, doi: <https://doi.org/10.1007/s10494-015-9622-4>.
- [18] F. Menter, R. Langtry and S. Volker, “Transition Modelling for General Purpose CFD,” *Flow, Turbulence and Combustion*, Vol. 77, No. 1, 2006, pp. 202–277, doi: <https://doi.org/10.1007/s10494-006-9047-1>.
- [19] R. Nichols, “Addition of a Local Correlation-Based Boundary Layer Transition model to the CREATETM-AV Kestrel Unstructured Flow Solver,” 2019, AIAA Paper 2019-1343, 2019 AIAA SciTech Forum, Jan. 7–11, San Diego, CA. doi: <https://doi.org/10.2514/6.2019-1343>.
- [20] J. Coder, “Further Development of the Amplification Factor Transport Transition Model for Aerodynamic Flows,” AIAA Paper 2019-0039, 2019 AIAA SciTech Forum, Jan. 7–11, San Diego, CA. doi: <https://doi.org/10.2514/6.2019-0039>.
- [21] L. Mack, “Transition and Laminar Instability,” 1977, NASA CR-153203.
- [22] Z. Yang and D. Mavriplis, “Implementation of Transition Modeling for Analysis and Optimization of Two-Dimensional Airfoil Problems,” AIAA Paper 2019-0293, 2019 AIAA SciTech Forum, Jan. 7–11, San Diego, CA. doi: <https://doi.org/10.2514/6.2019-0294>.

- [23] W. Valarezo and D. Mavriplis, “Navier-Stokes Applications to High-Lift Airfoil Analysis,” *Journal of aircraft*, Vol. 32, No. 3, 1995, pp. 618–624, doi: <https://doi.org/10.2514/3.46764>.
- [24] P. Spalart and S. Allmaras, “A One-Equation Turbulence Model for Aerodynamic Flow,” *Recherche Aerospaciale*, 1994, pp. 5–21, doi: <https://doi.org/10.2514/6.1992-439>.
- [25] D. Mavriplis, “An Advancing Front Delaunay Triangulation Algorithm Designed for Robustness,” *Journal of Computational Physics*, Vol. 117, No. 1, 1995, pp. 90–101, doi: <https://doi.org/10.1006/jcph.1995.1047>.
- [26] K. Mani and D. Mavriplis, “Unstructured Mesh Solution Techniques Using the NSU3D Solver,” 2014, AIAA Paper 2014-0081, 52nd Aerospace Sciences Meeting, January 2014. doi: <https://doi.org/10.2514/6.2014-0081>.
- [27] M. Park, K. Laflin, M. Chaffin, N. Powell and D. Levy, “CFL3D, FUN3D, and NSU3D Contributions to the Fifth Drag Prediction Workshop,” *Journal of Aircraft*, Vol. 51, No. 4, July 2014, pp. 1268–1283, doi: <https://doi.org/10.2514/1.C032613>.
- [28] D. Mavriplis, M. Long, T. Lake and M. Langlois, “NSU3D Results for the Second AIAA High Lift Prediction Workshop,” *Journal of Aircraft*, Vol. 52, No. 4, Aug. 2015, pp. 1063–1081, doi: <https://doi.org/10.2514/1.C033042>.
- [29] D. Mavriplis, Z. Yang and M. Long, “Results Using NSU3D for the First Aeroelastic Prediction Workshop,” AIAA Paper 2013-0786, 51st AIAA Aerospace Sciences Meeting, Jan. 7-10, 2013, Dallas/FT. Worth, TX. doi: <https://doi.org/10.2514/6.2013-786>.
- [30] D. Mavriplis, Z. Yang, and E. Anderson, “Development of an Analysis and Optimization Tool for Slotted Wing Natural-Laminar-Flow Aircraft,” AIAA Paper 2020-1292, 2020 AIAA SciTech Forum, Jan 6-10, Orlando, FL. doi: <https://doi.org/10.2514/6.2020-1292>.
- [31] R. Petzold and R. Radespiel, “Transition on a Wing with Spanwise Varying Crossflow and Linear Stability Analysis,” *AIAA Journal*, Vol. 53, No. 2, Feb. 2015, pp. 321–335, doi: <https://doi.org/10.2514/1.J053127>.
- [32] Z. Yang and D. Mavriplis, “Improved Fluid-Structure Interface for Aeroelastic Computations with Non-Matching Outer Mold Lines,” AIAA Paper 2021-0844, 2021 AIAA SciTech Forum, Virtual Event, Jan 2021. doi: <https://doi.org/10.2514/6.2021-0844>.
- [33] M. Bradley and C. Droney, “Subsonic Ultra Green Aircraft Research: Phase 2. Volume 2; Hybrid Electric Design Exploration,” NASA/CR-2015-218704/Volume II, NASA Langley Research Center, Hampton, VA, April 2015.
- [34] L. Metkowski and M. Maughmer, “Winglet and Strut Configuration Study for a Slotted, Natural-Laminar-Flow Strut-Braced Transport Aircraft,” AIAA Paper 2021-0843, AIAA Scitech Forum 2021, Virtual event, January 2021. doi: <https://doi.org/10.2514/6.2021-0843>.
- [35] K. Pham, L. Chou, N. Harrison, P. Vijgen, and A. Khodadoust, “Update on the Aerodynamic Performance Analysis of a Slotted Natural Laminar Flow Enabled Transonic Truss-Braced Wing,” 2023, AIAA Paper 2023-XXXX, To be presented at AIAA SciTech Forum, National Harbor, MD., Jan 23-27, 2023.

This article has been cited by:

1. Khanh H. Pham, Leo L. Chou, Neal A. Harrison, Paul M. Vijgen, Abdollah Khodadoust. Update on the Aerodynamic Performance Analysis of a SNLF-enabled Transonic Truss Braced Wing . [\[Abstract\]](#) [\[PDF\]](#) [\[PDF Plus\]](#)